MicroRNA-dependent regulation of biomechanical genes establishes tissue stiffness homeostasis

Albertomaria Moro [1,11], Tristan P. Driscoll [1,11], Liana C. Boraas[1], William Armero[1], Dionna M. Kasper[1], Nicolas Baeyens[2,3], Charlene Jouy[3], Venkatesh Mallikarjun[3,4], Joe Swift [3,4], Sang Joon Ahn[1], Donghoon Lee [5,6], Jing Zhang[5,6], Mengting Gu[5,6], Mark Gerstein[5,6,7], Martin Schwartz [1,3,8]* and Stefania Nicoli [1,9,10]*

Vertebrate tissues exhibit mechanical homeostasis, showing stable stiffness and tension over time and recovery after changes in mechanical stress. However, the regulatory pathways that mediate these effects are unknown. A comprehensive identification of Argonaute 2-associated microRNAs and mRNAs in endothelial cells identified a network of 122 microRNA families that target 73 mRNAs encoding cytoskeletal, contractile, adhesive and extracellular matrix (CAM) proteins. The level of these microRNAs increased in cells plated on stiff versus soft substrates, consistent with homeostasis, and suppressed targets via microRNA recognition elements within the 3′ untranslated regions of CAM mRNAs. Inhibition of DROSHA or Argonaute 2, or disruption of microRNA recognition elements within individual target mRNAs, such as connective tissue growth factor, induced hyper-adhesive, hyper-contractile phenotypes in endothelial and fibroblast cells in vitro, and increased tissue stiffness, contractility and extracellular matrix deposition in the zebrafish fin fold in vivo. Thus, a network of microRNAs buffers CAM expression to mediate tissue mechanical homeostasis.

Cells sense physical forces, including the stiffness of their extracellular matrix (ECM), through mechanosensitive integrins, their associated proteins and actomyosin. These components transduce physical forces into biochemical signals that regulate gene expression and cell function[1–3]. Tissues maintain nearly constant physical properties in the face of growth, injury, ECM turnover and altered external forces (for example, from blood pressure, tissue hydration or body weight)[1,4,5]. These effects imply tissue mechanical homeostasis, in which cells sense mechanical loads, due to both external and internal forces, and adjust their rates of matrix synthesis, degradation and organization to keep tissue properties constant. Cell contractility is critical in this process, as it is a key component of both the stiffness-sensing regulatory pathways and the matrix assembly process that governs resultant matrix properties, including stiffness[2,6].

Mechanical homeostasis requires that integrin mechanotransduction pathways mediate negative-feedback regulation of the contractile and biosynthetic pathways to maintain optimal tissue stiffness. That is, too soft or low force triggers increased matrix synthesis and contractility, whereas too stiff or high force triggers the opposite. However, in vitro studies have mainly elucidated positive-feedback (or feed forward) circuits, in which rigid substrates or high external forces increase actomyosin contraction, focal adhesions and ECM synthesis[7]. This type of mechanotransduction signalling characterizes fibrotic tissues, in which sustained contractility and excessive ECM compromise tissue function. Very little is known

about negative-feedback pathways that are critical to establish proper stiffness or contractility in normal, healthy tissues.

microRNAs (miRNAs) are processed via the ribonucleases DROSHA/DGCR8 and DICER[8] into mature 20–21 nucleotide (nt) RNA that recognize abundant and conserved 7–8 nt miRNA responsive elements (MREs) within mRNAs. MREs reside mainly in the 3′ untranslated regions (3′ UTRs) of mRNAs and base pair with the 5′ miRNA mature sequence (SEED region)[9]. The miRNA–MRE pairs are recognized by the Argonaute 2 (AGO2) protein complex, resulting in mRNA destabilization and/or reduced protein expression[8]. Thus, miRNAs can buffer fluctuations in protein levels caused by changes in transcriptional inputs or extracellular factors.

Although miRNAs participate in regulatory feedback loops that contribute to homeostasis in multiple contexts[10–12], their role in mechanical homeostasis is currently untested. Here, we describe a miRNA–CAM (cytoskeletal–actin–matrix) mRNA regulatory network that counteracts the effects of the ECM stiffness to promote the mechanical stability of cells and tissues, in both in vitro and in vivo models.

Results

miRNAs preferentially bind to CAM 3′ UTRs. To investigate potential roles for miRNAs in mechanical homeostasis, we analysed miRNA–mRNA interactions transcriptome wide using an AGO2-HITS-CLIP (high-throughput sequencing of RNA isolated by cross-linking immunoprecipitation) approach[13]. AGO2-bound miRNAs

[1]Yale Cardiovascular Research Center, Department of Internal Medicine, Section of Cardiology, Yale University School of Medicine, New Haven, CT, USA. [2]Laboratoire de Physiologie et Pharmacologie, Faculty of Medicine, Université Libre De Bruxelles, Brussels, Belgium. [3]Wellcome Trust Centre for Cell-Matrix Research, University of Manchester, Manchester, UK. [4]Division of Cell Matrix Biology and Regenerative Medicine, School of Biological Sciences, Faculty of Biology, Medicine and Health, Manchester Academic Health Science Centre, University of Manchester, Manchester, UK. [5]Program in Computational Biology and Bioinformatics, Yale University, New Haven, CT, USA. [6]Department of Molecular Biophysics and Biochemistry, Yale University, New Haven, CT, USA. [7]Department of Computer Science, Yale University, New Haven, CT, USA. [8]Departments of Cell Biology and Biomedical Engineering, Yale University, New Haven, CT, USA. [9]Department of Genetics, Yale University School of Medicine, New Haven, CT, USA. [10]Department of Pharmacology, Yale University School of Medicine, New Haven, CT, USA. [11]These authors contributed equally: Albertomaria Moro, Tristan Discroll. *e-mail: martin.schwartz@yale.edu; stefania.nicoli@yale.edu

or mRNAs were isolated from two unrelated human endothelial cell types, which are known to respond to mechanical forces, including ECM loads[3,14]. We exposed cultured human umbilical artery endothelial cells (HUAECs) and human umbilical vein endothelial cells (HUVECs) to UV light to crosslink protein–RNA complexes. Subsequently, we immunoprecipitated AGO2–RNA complexes, digested unbound RNA (schematic in Fig. 1a) and prepared complementary DNA libraries containing small (~30 nt AGO2–miRNA) and large RNAs (~70 nt AGO2–target mRNA) (Supplementary Fig. 1a). To identify conserved AGO2-binding sites, we performed high-throughput sequencing of three libraries for each cell type and selected sequence reads shared in all six samples. We aligned these AGO2-binding sites to human miRNA and genome databases and identified 30–70-nt intervals (peaks) significantly enriched above background ($P < 0.05$; Supplementary Fig. 1a and Methods). This analysis uncovered 316 AGO2-binding peaks within the 3′ UTRs of 127 human genes. These peaks were preferentially located right after the stop codon or right before the polyadenylation site (Fig. 1b and Supplementary Table 1), consistent with the enrichment of regulatory miRNA-binding sites that destabilize mRNAs[15]. Importantly, the human AGO2-binding peaks within these 30–70-nt sequences were highly conserved across hundreds of species (Fig. 1b), suggesting functional importance.

Gene Ontology (GO) analysis of AGO2-bound transcripts revealed that 73 of the 127 target mRNAs encode actin- and microtubule-associated proteins, focal adhesion proteins, ECM proteins and functionally related regulatory proteins (Fig. 1c and Supplementary Fig. 1b). We termed this group the CAM genes. The dramatic enrichment of CAM transcripts in the AGO2 complex is not accounted for by their abundance; indeed, the most transcriptionally active genes in cultured endothelial cells pertained to cell division (Supplementary Fig. 1b), which were under-represented in the identified AGO2-binding transcripts. No significant GO terms were associated with the remaining genes identified from the AGO2-HITS-CLIP.

We then searched for specific MRE sequences in AGO2 peaks localized in the 3′ UTRs of the CAM transcripts. We identified 122 miRNA families from AGO2-HITS-CLIP (Supplementary Table 2) that recognize one or more AGO2-CAM MREs (Fig. 1c and Supplementary Table 3). Cytoscape software revealed a highly interconnected network of miRNAs binding to CAM transcripts (Fig. 1c). Altogether, these data reveal pervasive miRNA-mediated post-transcriptional regulation of multiple CAM genes in endothelial cells.

Post-transcriptional regulation of CAM genes is sensitive to matrix stiffness. CAM proteins are highly conserved and play crucial roles in virtually every cell type as determinants of ECM organization and tissue stiffness[16]. This important function led us to hypothesize that the CAM mRNA–miRNA regulome is mechanosensitive. To test this, we plated endothelial cells on substrates of varying stiffness and used a Sensor-seq strategy[17] to assess post-transcriptional regulation mediated by 97 selected MREs within 51 different CAM 3′ UTRs (Supplementary Table 4). For this purpose, we created a 'CAM sensor library'. Each AGO2–3′ UTR peak containing at least one MRE was cloned downstream of an mCherry reporter in a bidirectional lentiviral vector[18] that co-expressed a green fluorescent protein (GFP) transcript lacking a 3′ UTR (schematic in Fig. 2a). Thus, miRNAs that target the MRE reduce mCherry levels, leading to a decreased mCherry/GFP ratio. Endothelial cells infected with this CAM sensor library at low levels (to avoid multiply infected cells) were seeded for 48 h on substrates with a rigidity of 3 kPa or 30 kPa, which approximate 'soft' and 'rigid' tissues[19], respectively (Supplementary Fig. 2a). miRNA activity on the MRE sensors was compared with the steady-state level of CAM proteins, as well as the expression of CAM RNAs and miRNAs,

in the same cellular settings. Thus, proteomics, RNA and miRNA sequencing were assessed in parallel.

To evaluate CAM sensor reporters, endothelial cells were separated by fluorescence-based sorting into bins according to the mCherry/GFP ratio, using an empty sensor as a negative control (not suppressed) and a miR-125 sensor as a positive control (strongly suppressed). Thus, bins were defined as 'strongly suppressed', 'suppressed', 'mildly suppressed' and 'not suppressed' relative to these internal standards (Fig. 2b). Wild-type (WT) endothelial cells expressing the CAM sensor library showed a broad distribution between the suppressed and not suppressed bins, on both soft and stiff substrates (Fig. 2b). Importantly, clustered regularly interspaced short palindromic repeats (CRISPR)–CRISPR-associated protein 9 (Cas9)-mediated disruption of AGO2 diminished the miRNA levels in endothelial cells (Supplementary Fig. 2b,c) and significantly increased the population of 'not suppressed' cells (Supplementary Fig. 2d). Thus, miRNAs are required for post-transcriptional inhibition of CAM sensors.

Sensor vectors from sorted cells were then isolated from each bin and barcoded using PCR primers that recognized each cloned CAM MRE and were compatible with high-throughput sequencing. Combining global miRNA profiling (Supplementary Table 7) and MRE reads from Sensor-seq revealed strong correlations between suppression of CAM sensors and the level of the respective matching miRNAs (Fig. 2c). Notably, both miRNA levels and CAM reporter suppression were present on soft substrate at baseline and elevated in cells on stiff substrates (Fig. 2c). Interestingly, the levels of most CAM mRNA and respective proteins (Supplementary Table 5) were also generally higher in stiff conditions (Fig. 2c). These results suggest transcriptional co-regulation between miRNAs and CAM mRNA targets on stiff substrates. Thus, the CAM MRE–miRNA network has the characteristics of a mechanoregulatory buffer of structural protein-coding genes.

**Loss of miRNA biogenesis leads to endothelial cell contractility.** To evaluate the function of this miRNA regulatory network, we first examined endothelial cells lacking AGO2 or DROSHA, which have diminished miRNA levels[20] (Supplementary Fig. 2c). We stained cells for F-ACTIN, the focal adhesion marker PAXILLIN and the mechanosensitive transcription factor Yes-associated protein (YAP)[21], and also measured traction stresses using elastic substrates with embedded beads[22]. Relative to control cells, AGO2 mutant cells showed increased actin stress fibres, focal adhesions, YAP nuclear localization and traction stress on both 3- and 30-kPa substrates, as well as on polyacrylamide substrates over a wider range of stiffnesses (Fig. 3a and Supplementary Fig. 3a). Consistent with these observations, immunofluorescence analysis revealed that cell spreading and YAP nuclear activation were inversely correlated with AGO2 protein levels (Supplementary Fig. 3b). Endothelial cells lacking DROSHA were similarly hyper-adhesive and hyper-contractile, supporting that diminished miRNA levels are the primary cause of these effects (Fig. 3b). Complementary to this finding, proteomic analysis of endothelial cells lacking miRNAs showed increased levels of several CAM proteins, reminiscent of the increased CAM levels in endothelial cells plated on 30-kPa versus 3-kPa substrates (Fig. 3c and Supplementary Table 5). Together, these data show that the loss of miRNA-mediated suppression of mRNAs increases CAM protein levels and enhances endothelial cell contractility and adhesion.

Blocking individual CAM–miRNA interactions affects endothelial cell mechanotransduction. To further validate the function of the miRNA–CAM mRNA network, we disrupted individual CAM–miRNA interactions. We chose nine of the mechanosensitive CAM MREs (stars in Fig. 2c and Supplementary Table 6) in which the MRE was within 20 nt of a protospacer sequence and thus targetable by a guide RNA (gRNA) and Cas9. Genome-wide analyses of
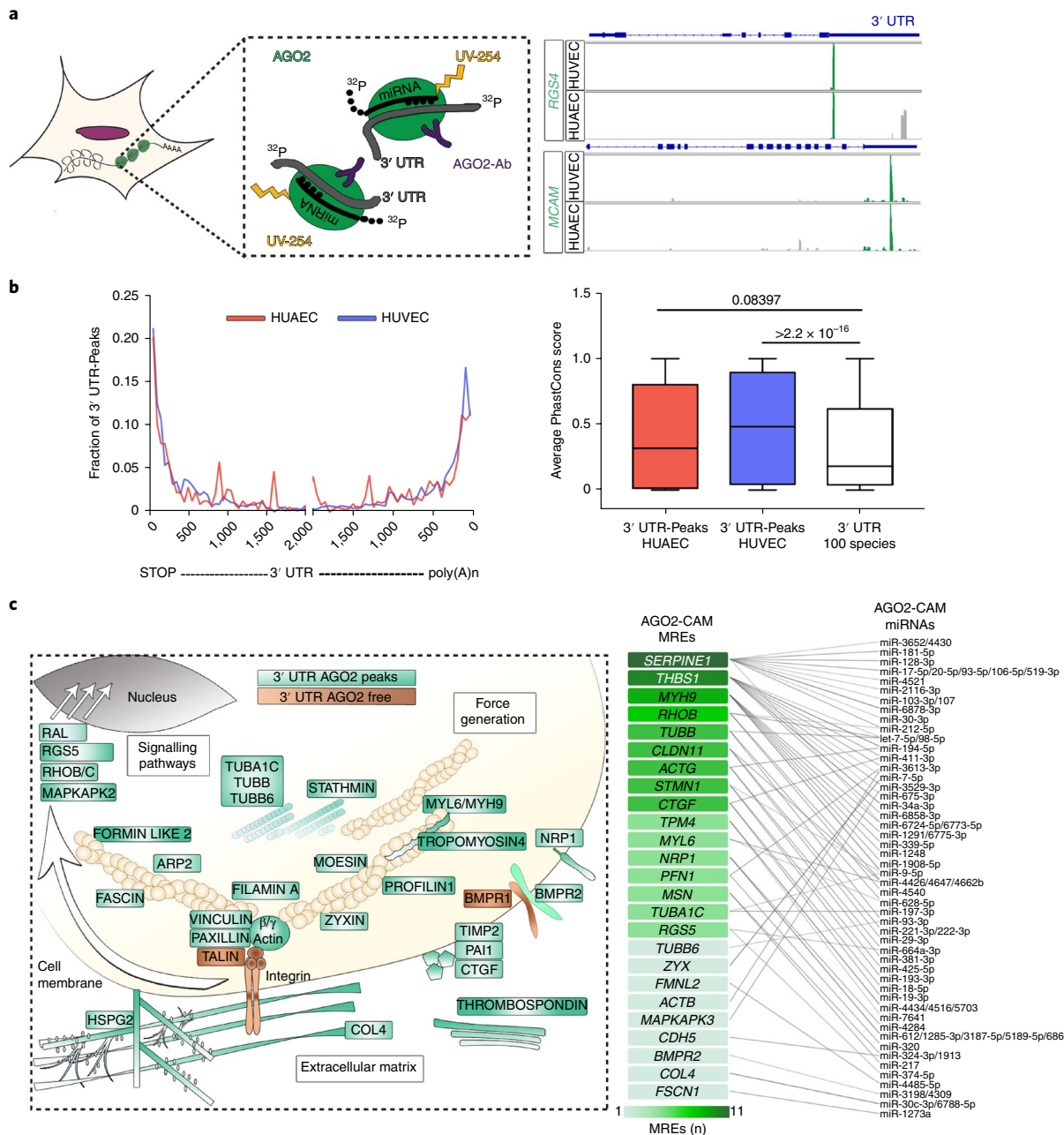
Fig. 1 | miRNAs regulate CAM genes. a, Left, schematic of AGO2-HITS-CLIP. miRNA–RNA complexes were crosslinked to AGO2 via UV light, and unbound RNAs were removed by RNase treatment. AGO2–RNA complexes were immunoprecipitated, and RNA was labelled with ^{32}P and isolated. Right, an Integrative Genomics Viewer display of HITS-CLIP reads showed the sequences aligned within 30–70-nt intervals (AGO2 peak) within the 3′ UTR region of the representative genes. Both HUAEC and HUVEC share the most significant peaks (green). Ab, antibody. **b**, Left, the chart represents positional enrichment of AGO2 peaks within the human 3′ UTR for HUAEC and HUVEC. The lines indicate the nucleotide positional distribution of peak sequences within meta-gene-analysed 3′ UTRs. Right, the box plot shows difference in conservation scores across samples scoring using PhastCons (Wilcoxon rank sum test). AGO2 peaks in HUAEC and HUVEC and binned human 3′ UTRs were compared with binned 3′ UTRs of 100 species. The conservation score is represented as a box plot with minimum, maximum, median and quartiles ($n = 3$ independent replica for HUVEC and HUAEC for a total of 383 for HUAEC, 749 for HUVEC and 125,685 for control individual value). **c**, Left, the schematic shows the CAM AGO2 regulome. AGO2–mRNA targets identified via AGO2-HIT-CLIP are highlighted in green. Integrins, TALIN1 and bone morphogenetic protein receptor 1 (BMPR1) proteins (brown) are part of the CAM's GO term but were not detected by AGO2-HITS-CLIP. Arrows point to downstream regulators of CAM proteins targeted by AGO2. CAM proteins and their regulators were identified by database searches (Supplementary Fig. 1a and Supplementary Tables 1–3) and manually curated for accuracy. Right, the chart shows the interactome for 25 of the 73 AGO2-CAM genes in which a complementary MRE (7–8 nt) was identified using Target Scan v.7.0 prediction software and miRNAs were identified from AGO2-HITS-CLIP reads using miRbase (Methods). Colour-coded boxes indicate the number of MREs identified in each of the selected CAM gene 3′ UTRs. The lines indicate interaction between MRE and miRNA family members with similar SEEDs. The mRNA–miRNA network shows high complexity, with numerous miRNAs binding to one or more CAM 3′ UTRs, whereas most CAM genes are targeted by more than one miRNA. ARP2, actin-related protein 2; COL4, collagen IV; HSPG2, heparan sulfate proteoglycan 2; MAPKAPK2, mitogen-activated protein kinase-activated protein kinase 2; MYH9, myosin 9; MYL6, myosin light polypeptide 6; NRP1, neuropilin 1; PAI1, plasminogen activator inhibitor 1; RGS5, regulator of G protein signalling 5; TIMP2, metalloproteinase inhibitor 2; TUBA1C, tubulin α-1C chain; TUBB, tubulin β-chain.
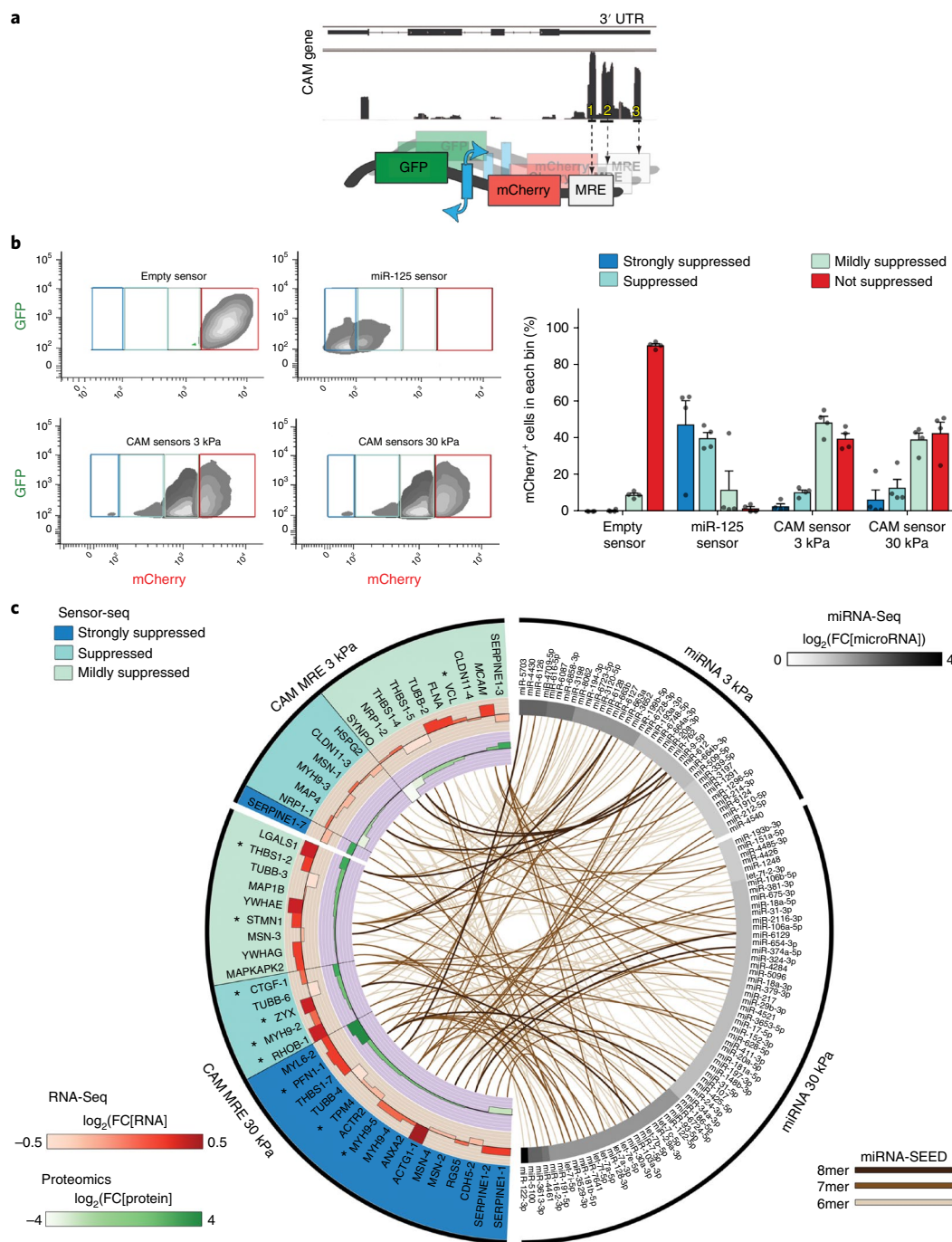
Fig. 2 | CAM MREs are actively repressed in stiff substrates. a, Schematic for the CAM sensor library. The Sensor-seq lentiviral library (Methods) consisted of (1) mCherry upstream of one of the 97 CAM MRE, and (2) GFP lacking any MRE (control). The numbered MREs indicate different MREs within one CAM 3′ UTR; alternatively, one MRE was cloned per CAM 3′ UTR (Supplementary Table 4). **b**, Left, mCherry and GFP intensities in HUVECs infected with the lentiviral library at 3 kPa and 30 kPa, a negative control (no MRE) and a positive control (3 perfect MREs for miR-125, abundant in HUVECs[45]). The density plots show the relative intensity of cell distribution using contour lines. Each contour line represents 15% probability (higher = lighter grey, lower = darker grey) of containing cells in each bin over total cells (10,000 cells). Sensor-seq library-infected HUVECs at 3 kPa and 30 kPa were sorted into 4 bins, as indicated, based on mCherry/GFP expression relative to controls. Cells in each bin were isolated and genotyped using a specific Illumina primer for sequencing (Methods). Right, the bar graph shows the percentage of mCherry+ cells sorted in each bin from four experiments (mean ± s.e.m.; single experiments are represented by dots). **c**, CIRCOS[46] graphical representation of CAM miRNA–MRE interactions. Right quadrants: endothelial cell miRNAs with putative SEED matching to CAM MREs sensors displaying differential gene expression between 3 kPa and 30 kPa, divided into 2 groups: expressed at 3 kPa compared to 30 kPa (black line, top right) and expressed at 30 kPa compared to 3 kPa (black line, bottom right). Left quadrants: CAM sensors most suppressed at 30 kPa compared to 3 kPa (black line, bottom left) and vice versa (black line, top left). The colour-coded boxes indicate the categorized bins in **b** at which cells were isolated and genotyped for a specific CAM sensor. The lines indicate a match between individual miRNA (SEED) and CAM MRE in each condition. The colour code indicates the level of complementarity between miRNA SEED and MRE nucleotides. The internal circles show the respective CAM RNAs (red) and proteins (green) log₂ fold change (FC) at 3 kPa compared to 30 kPa and 30 kPa compared to 3 kPa (Supplementary Tables 5 and 6). Asterisks indicate genes that were further validated with MRE targeting guide RNAs in Fig 4. Source data can be found in Supplementary Table 8.
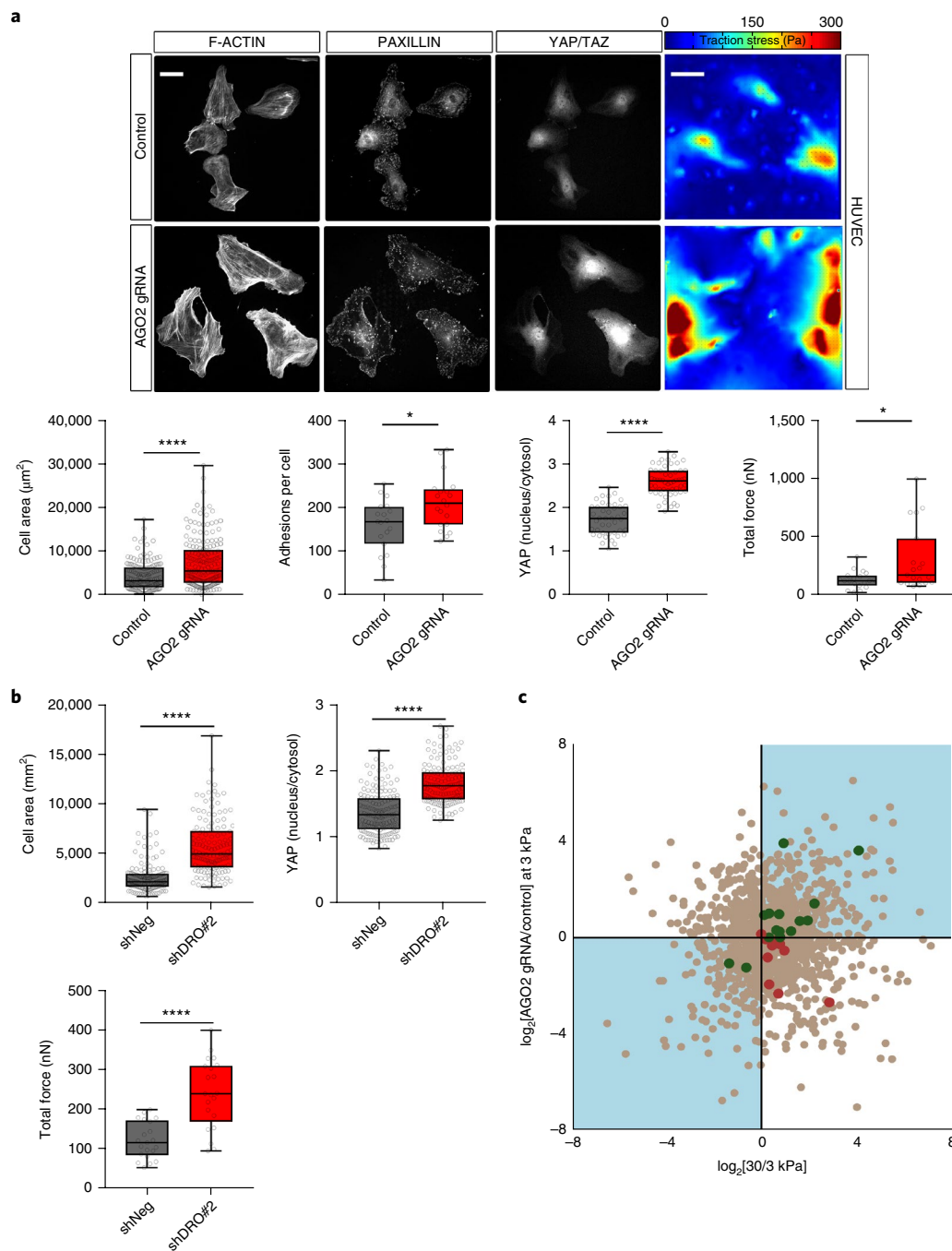
Fig. 3 | miRNAs limit endothelial cell spreading, YAP signalling and contractility. a, Representative immunofluorescence images and traction force maps of HUVECs after infection with AGO2 or a non-targeting control pLentiCRISPR virus. Cells on fibronectin-coated 3-kPa PDMS gels were stained for F-ACTIN (phalloidin), focal adhesions (PAXILLIN) and YAP/TAZ (scale bar, 50 μm). Heat maps of traction stress for single cells (scale bar, 20 μm) are also shown. All box plots show the minimum, maximum, median and quartiles. Cell area (based on phalloidin staining) (control: $n = 163$; AGO2 gRNA: $n = 182$ cells per group; dots indicate individual cells, representative data from 6 independent experiments, ****$P < 0.0001$, unpaired, two-sided t-test), the number of PAXILLIN adhesions per cell (control: $n = 19$ fields of view 49 cells; AGO2 gRNA: $n = 20$ fields of view 51 cells; dots indicate the average per field of view, representative data from 3 independent experiments, *$P = 0.0085$, unpaired, two-sided t-test) and nuclear-to-cytoplasmic ratio of YAP/TAZ (control: $n = 43$ cells; AGO2 gRNA: $n = 54$ cells; dots represent single-cell measurements, representative data from 2 independent experiments, ****$P < 0.0001$, unpaired, two-sided t-test). The box plot for total force shows total force per single cell ($n = 19$ cells per group; dots indicate individual cells, from 2 independent experiments, *$P = 0.0119$, unpaired, two-sided t-test). **b**, Box plots show quantification of HUVEC treated with shRNA against DROSHA (Methods) and seeded on fibronectin-coated 3-kPa PDMS gels for the cell spread area (shNeg: $n = 156$; shDRO#2: $n = 138$ cells, from two independent experiments, ****$P < 0.0001$, unpaired, two-sided t-test), YAP nuclear localization (shNeg: $n = 156$; shDRO#2: $n = 138$ cells, from 2 independent experiments, ****$P < 0.0001$, unpaired two-sided t-test) and total force per cell ($n = 21$ cells per group, from 2 independent experiments, ****$P < 0.0001$, unpaired, two-sided t-test). **c**, Scatter plot representing the difference in protein expression between HUVEC seeded on 30 kPa versus 3 kPa (x axis) or between HUVECs infected with AGO2 gRNA versus control gRNA (y axis) ($n = 3$ replicates). Green and red identify CAM proteins with coherent or incoherent differential expression, respectively (Supplementary Table 6). Source data can be found in Supplementary Table 8.
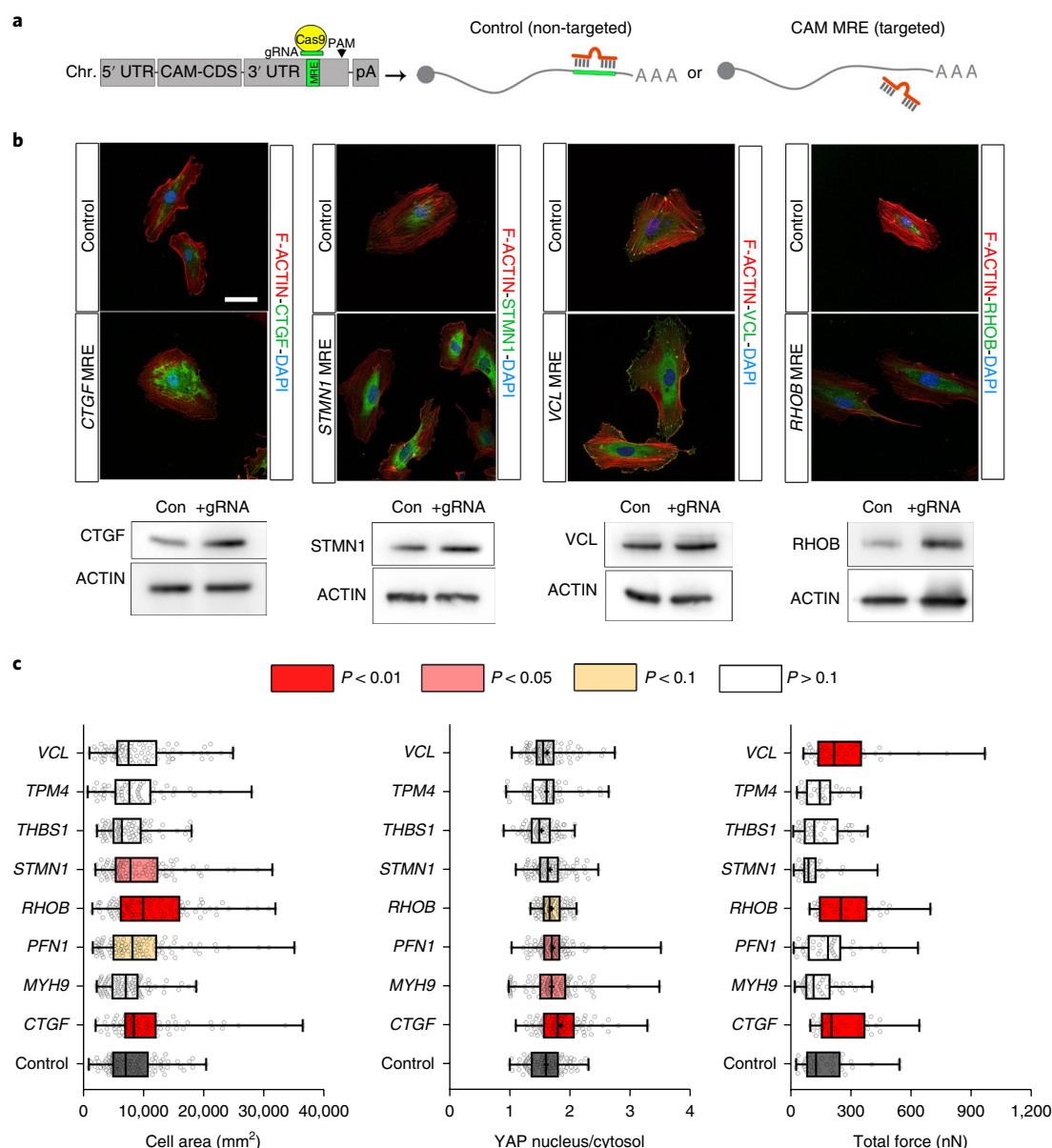
Fig. 4 | Post-transcriptional regulation of individual CAM genes limits endothelial cell spreading, YAP signalling and/or contractility. a, Experimental strategy to mutate individual MREs in CAM genes 3′ UTRs to block miRNA binding (see Methods and Supplementary Fig. 2b). CDS, coding sequence; Chr. chromosome; pA, poly A; PAM, protospacer adjacent motif. **b**, Representative immunofluorescence images (top; scale bar, 50 μm) and western blot (bottom) of CAM proteins as indicated (CTGF: ~37 kDa, stathmin (STMN1): ~19 kDa, vinculin (VCL): ~116 kDa, RHOB: ~25 kDa, ACTIN: ~47 kDa). HUVECs were infected with lentivirus carrying Cas9 and gRNA targeting specific CAM MREs and no-target gRNA (**a**) and processed at 7 d post-infection. **c**, Quantification of cell spreading ($n = 99, 75, 91, 94, 88, 87, 79, 54$ and 83 from the bottom to the top, representative data from 2 independent experiments), YAP nuclear translocation ($n = 91, 81, 87, 93, 79, 88, 67, 54$ and 84 cells from the bottom to the top, representative data from 2 independent experiments) and total force per cell ($n = 38, 33, 37, 36, 34, 34, 34, 30$ and 36 cells from the bottom to the top, from 2 independent experiments) in HUVECs on 3-kPa PDMS gels for 48 h after mutation of the indicated MREs (all box plots indicate the minimum, maximum, median and quartiles, single dots represent single cells, colours represent P values, one-way ANOVA with Fisher's least significant difference). Source data can be found in Supplementary Table 8.

CAM MREs in endothelial cells treated with gRNA–CRIPSR–Cas9 revealed that nearly 75% of insertions and deletions were within the desired MRE region (± 20 bp) (Fig. 4a and Supplementary Fig. 4a). To test whether MRE-proximal mutations increased the expression of the cognate proteins, we analysed CAM protein levels via immunofluorescence and western blot. Individual CAM levels increased in the respective MRE mutants compared to control cells (Fig. 4b), consistent with loss of miRNA-mediated suppression[23].

Finally, we tested the mechanical properties of each CAM MRE mutant population and found, to varying extents, that cell area,

YAP nuclear localization and/or traction stresses were significantly higher than control targeted cells (Fig. 4c).

Whereas multiple genes clearly contributed to each effect, the gene whose MRE mutation gave the most consistent results across multiple assays was *CTGF* (encoding connective tissue growth factor). CTGF is a matrix protein that modulates the interaction of cells with the ECM[24], suggesting that it is a component of a protein-based regulatory network and probably functions via receptor-mediated signalling to control these functions. Blocking CTGF miRNA repression in endothelial cells via a target protector RNA
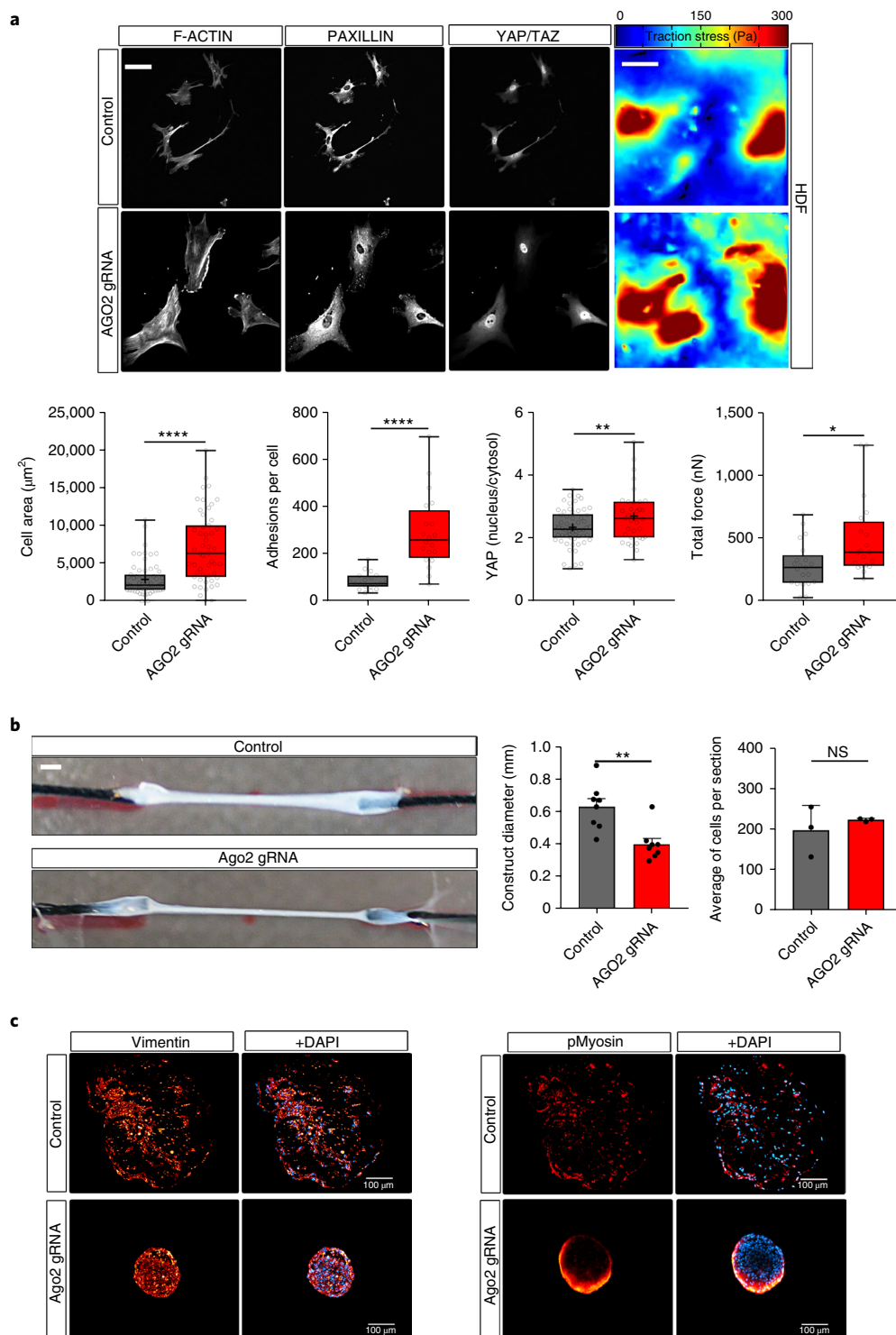
Fig. 5 | AGO2 activity is required to limit fibroblast contractility in 2D and 3D models. a, Representative immunofluorescence images of HDF after infection with the pLentiCRISPR virus directed at *AGO2* or a non-targeting control seeded on fibronectin-coated 3-kPa PDMS gels for 48 h (scale bar, 50 μm). Heat maps of traction stress for single cells are also shown (scale bar, 20 μm). Box plots show the HDF cell area (control: $n = 63$ cells; AGO2 gRNA: $n = 51$ cells, representative data from 4 independent experiments, ****$P < 0.001$, unpaired, two-sided t-test) based on phalloidin staining, the number of PAXILLIN adhesions per cell ($n = 19$ fields of view 63 cells; AGO2: $n = 20$ fields of view 51 cells; dots indicate the average per field of view; representative data from 2 independent experiments, ****$P < 0.0001$, unpaired, two-sided t-test) and the nuclear-to-cytoplasmic ratio of YAP/TAZ (control: $n = 58$ cells; AGO2 gRNA: $n = 34$, cells are represented by single dots; representative data from 2 independent experiments, **$P = 0.0174$, unpaired, two-sided t-test). Single-cell maps of traction stress and quantification of total force per cell (box plots with whiskers indicate the minimum and maximum values with median and quartiles, control: $n = 21$ cells, AGO2 gRNA: $n = 20$ cells; *$P = 0.0109$, unpaired, two-sided t-test). **b**, Representative 3D matrix constructs with control or Ago2-mutated mouse dermal fibroblasts (scale bar, 1 mm). Bar plots show the average cell number and construct diameter within transverse sections ($n = 8$, bars indicate the mean ± s.e.m. and dots represent single replicate, **$P < 0.01$, NS, not significant). **c**, Transverse sections of control and Ago2-depleted matrix constructs stained for vimentin or pMyosin and DAPI. Source data can be found in Supplementary Table 8.
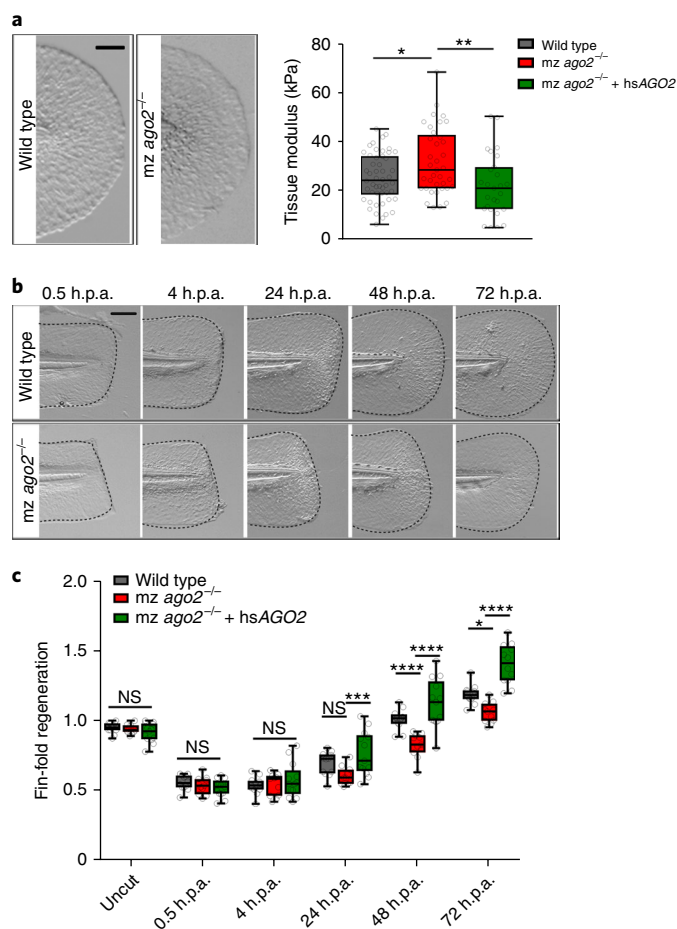
Fig. 6 | Ago2 activity is required for tissue stiffness and wound healing in the zebrafish fin-fold regeneration assay. a, Left, bright-field images of 48 h.p.f. fin-fold tissues in the indicated genotypes (scale bar, 0.05 mm). Right, elastic modulus of 48 h.p.f. zebrafish fin-fold surfaces of WT, mz $ago2^{-/-}$ and mz $ago2^{-/-}$ rescued with 200 pg of in vitro-transcribed human WT *AGO2* mRNA (hs*AGO2* mRNA). Embryos were harvested and adhered to a soft surface of PDMS in egg water. Elastic moduli were measured with AFM using NanoScope Analysis 1.5 software to fit force-deflection curves using the Sneadon model. At least 2 fin-fold regions within each of 10–11 embryos were tested for each genotype (WT: $n=50$, mz $ago2^{-/-}$: $n=37$, mz $ago2^{-/-}$+hs*AGO2*: $n=27$ measurements; box plots indicate minimum, maximum, median and quartiles, single measures are represented by dots, combined data from 4 independent experiments, $*P=0.0284$, $**P=0.0033$, one-way ANOVA with Tukey's multiple comparisons test). **b**, Bright-field images of zebrafish fin folds at the indicated stages and genotypes (the head is to the left; scale bar, 0.1 mm). The dotted black line outlines the edge of the fin fold. Fin-fold regeneration was assessed from the distance between the wound edge and the embryo body. One-cell stage WT, mz $ago2^{-/-}$ and mz $ago2^{-/-}$ embryos rescued with 200 pg of hs*AGO2* mRNA. Values were normalized for the size of the fin fold prior to injury (WT: $n=12$, mz $ago2^{-/-}$: $n=11$, mz $ago2^{-/-}$: $n=13$ fish from 2 independent experiments, box plots indicate minimum, maximum, median and quartiles, dots indicate single-fish measurements, $*P=0.0168$, $***P=0.0038$; $****P<0.0001$, two-way ANOVA with Sidak's multiple comparisons test). Source data can be found in Supplementary Table 8.

oligonucleotide or MRE mutation had similar effects (Fig. 4c and Supplementary Fig. 4b), providing independent support. Notably, no single CAM MRE mutation reproduced the strong phenotype observed after AGO2 downregulation, suggesting that a network of

miRNA–CAM mRNA interactions mediates mechanical homeostasis in cells.

miRNA-dependent regulation limits contractility in 2D and 3D fibroblast models. We next tested the generality of the identified miRNA–CAM gene regulations using fibroblasts as a second model system. Profiling of miRNAs in human dermal fibroblasts (HDFs) seeded on 3- versus 30-kPa substrates showed that miRNAs targeting CAM genes are upregulated on stiff substrates similarly to endothelial cells (Supplementary Fig. 5a and Supplementary Table 7). Depletion of AGO2 in HDFs also increased F-ACTIN and focal adhesion levels, traction forces and YAP localization compared to control cells (Fig. 5a and Supplementary Fig. 5b).

To determine whether the miRNA-mediated network functions at the tissue level, we examined primary mouse dermal fibroblasts in a 3D matrix. Cells suspended in attached fibrin gels contract and replace the fibrin with their own matrix over about 5 d (Fig. 5b), providing a 3D model of cell behaviour. Transduction of freshly isolated cells with a CRISPR–Cas9–gRNA virus targeting *Ago2* reduced Ago2 protein levels by ~50–60% (Supplementary Fig. 5c). Ago2-depleted fibroblasts in 3D matrix generated tissue constructs with reduced diameters but no significant change in cell numbers (Fig. 5b). Immunostaining transverse sections of these constructs confirmed the decreased diameter, based on staining with the cytoskeleton protein vimentin (Fig. 5c). Staining for phosphorylated myosin light chain was elevated, consistent with increased contractility (Fig. 5c). These data indicate that reducing miRNA-dependent regulation stimulates fibroblast contraction of the 3D matrix.

miRNA-dependent regulation controls tissue stiffness and wound healing in vivo. We next tested whether miRNAs regulate mechanical homeostasis in vivo using the zebrafish fin-fold regeneration model[25]. The fin fold is a non-vascularized appendage comprising a few layers of epidermis and fibroblast-like cells[26]. Wounding triggers a healing response mediated by a conserved and rapid matrix remodelling- and actomyosin-based process that involves the formation of a provisional matrix, inflammatory cell invasion, cell migration, proliferation and resolution[27].

To investigate miRNA-dependent regulation of mechanical homeostasis in zebrafish, we first examined embryos that carry a maternal zygotic homozygous mutation in *ago2* (mz $ago2^{-/-}$)[28], which show reduced levels of Ago2 and of miRNAs (Supplementary Fig. 6a). To evaluate miRNA activity in the fin fold, we co-injected an miRNA-sensitive GFP mRNA, containing three perfect miR-24 MREs within the 3′ UTR[29], with an miRNA-insensitive mCherry control mRNA. As expected, mz *ago2* mutants showed elevated levels of GFP, but not of mCherry, when compared to WT embryos, confirming reduced miRNA-mediated suppression (Supplementary Fig. 6b).

We then quantified tissue stiffness using atomic force microscopy (AFM)-based nanoindentation on the central region of the fin fold. The appearance of this tissue was indistinguishable between genotypes (Fig. 6a), ruling out obvious developmental defects. However, the elastic modulus was ~30% higher in mz $ago2^{-/-}$ than in WT embryos, indicating increased mechanical rigidity (Fig. 6a). Importantly, normal tissue stiffness was restored upon injection of in vitro transcribed mRNA encoding human AGO2 (hs*AGO2* mRNA), demonstrating that the stiffness of this tissue is dependent on the level of Ago2 (Fig. 6a). Following amputation, mz *ago2* mutants exhibited slower repair than WT embryos, which was rescued by hs*AGO2* mRNA (Fig. 6b). WT and mz $ago2^{-/-}$ wounds did not display differences in cell cycle progression, detected by proliferating cell nuclear antigen staining[30], or in apoptosis, detected by TdT-mediated dUTP nick end labelling (TUNEL)[31] assay (Supplementary Fig. 6c,d). These results support that miRNA-dependent suppression restrains tissue stiffness and contributes to tissue healing in vivo.
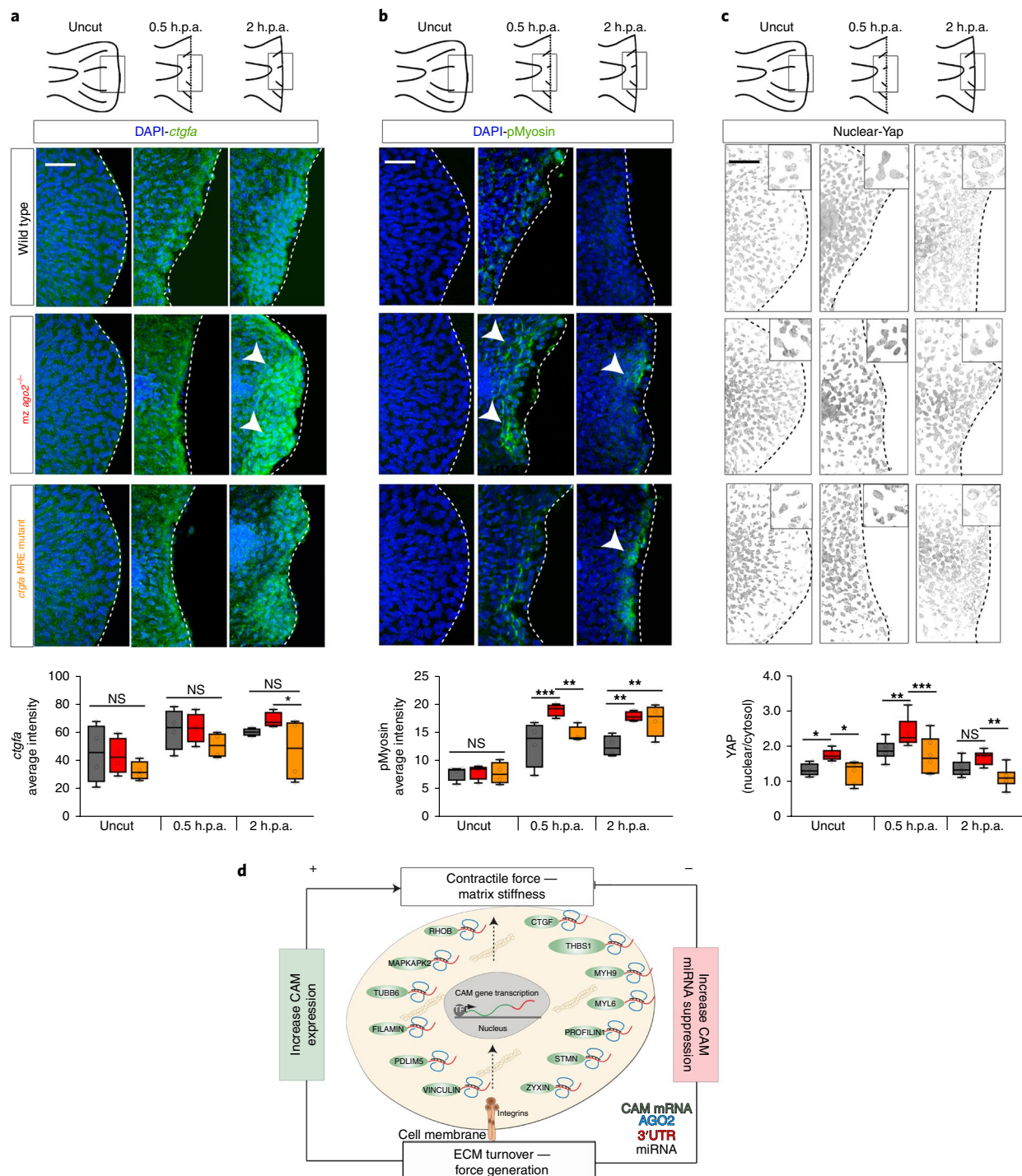
Fig. 7 | Wound healing in mz *ago2* and *ctgfa* MRE fin-fold mutants. a–c, Top, schematics representing the time course of fin-fold regeneration. Boxes identify the region of interest reported in the images below. Bottom, confocal images of whole-mount fin folds within the boxed region from the schematics at the top, at the indicated stages (scale bars, 120 µm). The white and black dotted lines indicate the edge of the fin fold. The white arrowheads point to staining for the indicated markers. The graphs show box plots with minimum, maximum, median and quartiles. Wild type, gray; mz *ago2*-/-, red; *ctgfa* MRE mutant, orange. Intensity profiles for multiple embryos were combined (CTGF: $n = 4$ embryos per genotype, * in mz *ago2*−/− 2 h versus *ctgfa* MRE 2 h = 0.0318 (**a**); pMyosin: $n = 4$ embryos per genotype, *** in WT 0 h versus mz *ago2*−/− 0 h = 0.0004, ** in mz *ago2*−/− 0 h versus *ctgfa* MRE 0 h = 0.0069, ** in WT 2 h versus mz *ago2*−/− 2 h = 0.0014, ** in WT 2 h versus *ctgfa* MRE 2 h = 0.0041 (**b**); YAP: $n = 6$ embryos for each genotype, * in WT uncut versus mz *ago2*−/− uncut = 0.027, * in ago uncut versus *ctgfa* MRE uncut = 0.0126, ** in WT 0 h versus mz *ago2*−/− 0 h = 0.0082, *** in mz *ago2*−/− 0 h versus *ctgfa* MRE 0 h = 0.0008, ** in ago 2 h versus *ctgf* 2 h = 0.0035 (**c**); single fish are represented by dots, NS, not significant, unpaired, two-sided *t*-test). For Yap, the protein nuclear localization was represented. The nucleus/cytosol ratio was obtained using the DAPI channel to generate a binary mask and subtract nuclear YAP-GFP intensity from the total YAP-GFP detected (see Methods and Supplementary Fig. 7b). **d**, Model for miRNA post-transcriptional regulation of structural protein function in mechanical tissue homeostasis. Increases in matrix stiffness and the resulting cell contractility increase integrin and actomyosin-dependent CAM signalling, which upregulates miRNAs that suppress CAM transcripts, thus restoring normal cell mechanics. PDLIM5, PDZ and LIM domain protein 5; TF, transcription factor; THBS1, thrombospondin 1. Source data can be found in Supplementary Table 8.

miRNA-dependent CAM gene regulation limits tissue contractility during wound healing. Wounding triggers increased contractility and matrix rigidity as a rapid, first response[32]. According to our notion of mechanical homeostasis, these changes should activate negative-feedback mechanisms that restore mechanical equilibrium[3]. Thus, we examined matrix, actomyosin activation and the mechanosensitive translocation of Yap[21] before and after wounding the zebrafish fin fold in the WT embryo versus the mz *ago2* mutant. As expected[27], WT embryos showed increased staining for pMyosin, Ctgfa and fibronectin[27,32] in the wound area between 0.5 and 2 h post-amputation (h.p.a.) (Fig. 7a,b and Supplementary Fig.7a). In comparison, mz *ago2*^{−/−} wounded fins showed strikingly elevated and persistent pMyosin staining at both 0.5 and 2 h.p.a., and higher levels of Ctgfa and fibronectin at 2 h.p.a. (Fig. 7a,b and Supplementary Fig. 7a). Consistent with the increase in tissue stiffness (Fig. 6a), mz *ago2*−/− showed higher basal Yap nuclear localization than WT embryos that further increased at 0.5 h.p.a. and persisted at 2 h.p.a. (Fig. 7c and Supplementary Fig. 7b). Thus, loss of miRNA-mediated suppression leads to an exaggerated mechanical response and impaired mechanical resolution during wound healing.

To correlate these effects with regulation of individual CAM genes, we generated zebrafish embryos carrying mutations in the two 3′ UTR MREs of the *ctgfa* gene (Supplementary Fig. 7c,d). These MREs are conserved in the human *CTGF* 3′ UTR, and their mutation had the largest effect in vitro (Fig. 4c). Accordingly, a GFP sensor mRNA bearing a *ctgfa* 3′ UTR fragment showed reduced expression in WT relative to mz *ago2*^{−/−} embryos, which required the MRE sites (Supplementary Fig. 7c). These results support miRNA-dependent inhibition of *ctgfa* via the MREs in zebrafish. Embryos with mutated *ctgfa* MREs showed persistent pMyosin activation compared to WT embryos by 2 h.p.a. (Fig. 7b), consistent with the induction of Ctgfa at 2 h.p.a. in the mz *ago2* mutant (Fig. 7a). However, no other differences were detected in the *ctgfa* MRE mutant embryos (Fig. 7a–c and Supplementary Figs. 6c,d and 7a,b). These results support that post-transcriptional regulation of *ctgfa* contributes to specific Ago2-mediated mechanical effects within the miRNA–CAM mRNA network.

Discussion

We report that an unbiased analysis of miRNAs and their target genes in endothelial cells, together with functional assays in several biological systems, reveal the existence of a mechanosensitive miRNA-based programme that counteracts cell adhesion, cytoskeletal, contractile and matrix protein expression. This system functions in several cell types, across multiple species, and appears to be conserved throughout vertebrate evolution. Importantly, most of the protein-coding genes for synthesis and assembly of stiff ECM are targeted by miRNAs that are upregulated on stiff substrates. Thus, a 'buffer' is generated, in which increased matrix stiffness upregulates both CAM gene transcription and the miRNAs that suppress these transcripts. This miRNA regulome has the molecular and functional characteristics of a homeostatic mechanism, in which changes in cell contraction and matrix are counteracted to maintain normal tissue stiffness (Fig. 7d).

Endothelial cells in vivo are also subject to wall stretch and fluid shear stress from blood pressure and blood flow, which were not examined here but which are likely to interact with cell responses to matrix stiffness. Interestingly, both of these variables are subject to negative-feedback regulation[4], consistent with the general importance of mechanical homeostasis. Although the current studies dissected the post-transcriptional regulation of CAM proteins in stiffness homeostasis, a deeper understanding of these mechanisms will need to address the interplay between RNA regulation, stiffness, shear stress in endothelial and other cells subject to external forces.

A network-mediated mechanism for stiffness homeostasis, rather than regulation of one or a few CAM genes, would be expected to increase the robustness of the system. Multiple miRNAs can regulate a large cohort of CAM genes via different MREs, whereas different cell types can do so by controlling the expression and processing of tissue-specific mature miRNAs[33–35]. However, we speculate that these miRNA networks are likely to be subelements within a larger and more robust network of negative and positive circuits, connected by multiple nodes, that mediate tissue homeostasis over the multiple decades of human life[36]. Such nodes could develop within a hierarchy of epigenetic factors in which, for example, the activation of YAP/TAZ and its direct target gene *CTGF*, may be one of the upstream components.

A role for miRNAs in tissue mechanical homeostasis is supported by the widespread deregulation of miRNAs during lung, renal, cardiac and liver fibrosis, including miRNAs that target ECM proteins[37–39]. Idiopathic lung fibrosis is also linked to reduced levels of miRNAs that target the ECM, cytoskeletal and transforming growth factor-β pathways genes[40–42]. All of these studies reported reduced levels of miR-29 species, in contrast to our finding that, in normal cells, miR-29 species are increased on stiff substrates. These results are consistent with the notion that fibrotic disease involves disruption of normal stiffness miRNA-dependent homeostasis[43].

Cells and tissues with impaired regulation of miRNAs upon AGO2 or DROSHA partial loss of function show defective adaptation to stiffness. The degree of such effects could be related to the corresponding miRNAs levels. Although model organisms that completely lack miRNAs do not develop properly, heterozygous mutants of Ago2 do not manifest obvious phenotypes[44]. Further studies will be necessary to test whether this model has tissue stiffness defects in normal conditions and/or respond abnormally to perturbations, such as wounding, or during ageing.

miRNA-dependent post-transcriptional regulation of structural proteins provides a concrete molecular mechanism that can explain how healthy tissues sustain optimal mechanical properties. Thus, these findings are an important step towards understanding the pathological alterations that result in fibrotic and related diseases. Characterizing the stiffness-dependent RNA metabolism of cytoskeleton and matrix transcripts, their possible regulation under other physical forces and elucidating the complete regulatory network that mediates long-term mechanical robustness are the essential tasks for future studies.

Online content

Any methods, additional references, Nature Research reporting summaries, source data, statements of data availability and associated accession codes are available at https://doi.org/10.1038/s41556-019-0272-y.

References

1. Cyron, C. J. & Humphrey, J. D. Growth and remodeling of load-bearing biological soft tissues. *Meccanica* **52**, 645–664 (2017).
2. Gilbert, P. M. & Weaver, V. M. Cellular adaptation to biomechanical stress across length scales in tissue homeostasis and disease. *Semin. Cell Dev. Biol.* **67**, 141–152 (2017).
3. Humphrey, J. D., Dufresne, E. R. & Schwartz, M. A. Mechanotransduction and extracellular matrix homeostasis. *Nat. Rev. Mol. Cell Biol.* **15**, 802–812 (2014).
4. Humphrey, J. D. Vascular adaptation and mechanical homeostasis at tissue, cellular, and sub-cellular levels. *Cell Biochem. Biophys.* **50**, 53–78 (2008).
5. Seki, E. & Brenner, D. A. Recent advancement of molecular mechanisms of liver fibrosis. *J. Hepatobiliary Pancreat. Sci.* **22**, 512–518 (2015).
6. Huang, S. & Ingber, D. E. Cell tension, matrix mechanics, and cancer development. *Cancer Cell* **8**, 175–176 (2005).
7. Sun, Z., Guo, S. S. & Fassler, R. Integrin-mediated mechanotransduction. *J. Cell Biol.* **215**, 445–456 (2016).

8. Pasquinelli, A. E. MicroRNAs and their targets: recognition, regulation and an emerging reciprocal relationship. *Nat. Rev. Genet.* **13**, 271–282 (2012).

9. Hafner, M. et al. Transcriptome-wide identification of RNA-binding protein and microRNA target sites by PAR-CLIP. *Cell* **141**, 129–141 (2010).

10. Herranz, H. & Cohen, S. M. MicroRNAs and gene regulatory networks: managing the impact of noise in biological systems. *Genes Dev.* **24**, 1339–1344 (2010).

11. Tsang, J., Zhu, J. & van Oudenaarden, A. MicroRNA-mediated feedback and feedforward loops are recurrent network motifs in mammals. *Mol. Cell* **26**, 753–767 (2007).

12. Kasper, D. M. et al. MicroRNAs establish uniform traits during the architecture of vertebrate embryos. *Dev. Cell* **40**, 552–565.e5 (2017).

13. Chi, S. W., Zang, J. B., Mele, A. & Darnell, R. B. Argonaute HITS-CLIP decodes microRNA–mRNA interaction maps. *Nature* **460**, 479–486 (2009).

14. Byfield, F. J., Reen, R. K., Shentu, T. P., Levitan, I. & Gooch, K. J. Endothelial actin and cell stiffness is modulated by substrate stiffness in 2D and 3D. *J. Biomech.* **42**, 1114–1119 (2009).

15. Grimson, A. et al. MicroRNA targeting specificity in mammals: determinants beyond seed pairing. *Mol. Cell* **27**, 91–105 (2007).

16. Saphirstein, R. J. & Morgan, K. G. The contribution of vascular smooth muscle to aortic stiffness across length scales. *Microcirculation* **21**, 201–207 (2014).

17. Mullokandov, G. et al. High-throughput assessment of microRNA activity and function using microRNA sensor and decoy libraries. *Nat. Methods* **9**, 840–846 (2012).

18. Kamata, M., Liang, M., Liu, S., Nagaoka, Y. & Chen, I. S. Live cell monitoring of hiPSC generation and differentiation using differential expression of endogenous microRNAs. *PLoS ONE* **5**, e11834 (2010).

19. Discher, D. E., Janmey, P. & Wang, Y. L. Tissue cells feel and respond to the stiffness of their substrate. *Science* **310**, 1139–1143 (2005).

20. Kim, Y. K., Kim, B. & Kim, V. N. Re-evaluation of the roles of DROSHA, Export in 5, and DICER in microRNA biogenesis. *Proc. Natl Acad. Sci. USA* **113**, E1881–E1889 (2016).

21. Dupont, S. et al. Role of YAP/TAZ in mechanotransduction. *Nature* **474**, 179–183 (2011).

22. Kumar, A. et al. Talin tension sensor reveals novel features of focal adhesion force transmission and mechanosensitivity. *J. Cell Biol.* **213**, 371–383 (2016).

23. Bassett, A. R. et al. Understanding functional miRNA–target interactions in vivo by site-specific genome engineering. *Nat. Commun.* **5**, 4640 (2014).

24. Shi-Wen, X., Leask, A. & Abraham, D. Regulation and function of connective tissue growth factor/CCN2 in tissue repair, scarring and fibrosis. *Cytokine Growth Factor Rev.* **19**, 133–144 (2008).

25. Kawakami, A., Fukazawa, T. & Takeda, H. Early fin primordia of zebrafish larvae regenerate by a similar growth control mechanism with adult regeneration. *Dev. Dyn.* **231**, 693–699 (2004).

26. Mathew, L. K. et al. Comparative expression profiling reveals an essential role for raldh2 in epimorphic regeneration. *J. Biol. Chem.* **284**, 33642–33653 (2009).

27. Mateus, R. et al. In vivo cell and tissue dynamics underlying zebrafish fin fold regeneration. *PLoS ONE* **7**, e51766 (2012).

28. Cifuentes, D. et al. A novel miRNA processing pathway independent of Dicer requires Argonaute2 catalytic activity. *Science* **328**, 1694–1698 (2010).

29. Amelio, I. et al. miR-24 triggers epidermal differentiation by controlling actin adhesion and cell migration. *J. Cell Biol.* **199**, 347–363 (2012).

30. Nechiporuk, A. & Keating, M. T. A proliferation gradient between proximal and msxb-expressing distal blastema directs zebrafish fin regeneration. *Development* **129**, 2607–2617 (2002).

31. Hasegawa, T. et al. Transient inflammatory response mediated by interleukin-1β is required for proper regeneration in zebrafish fin fold. *eLife* **6**, e22716 (2017).

32. Mateus, R. et al. Control of tissue growth by Yap relies on cell density and F-actin in zebrafish fin regeneration. *Development* **142**, 2752–2763 (2015).

33. Mori, M. et al. Hippo signaling regulates microprocessor and links cell-density-dependent miRNA biogenesis to cancer. *Cell* **156**, 893–906 (2014).

34. Chaulk, S. G., Lattanzi, V. J., Hiemer, S. E., Fahlman, R. P. & Varelas, X. The Hippo pathway effectors TAZ/YAP regulate dicer expression and microRNA biogenesis through Let-7. *J. Biol. Chem.* **289**, 1886–1891 (2014).

35. Davis, B. N., Hilyard, A. C., Lagna, G. & Hata, A. SMAD proteins control DROSHA-mediated microRNA maturation. *Nature* **454**, 56–61 (2008).

36. Felix, M. A. & Wagner, A. Robustness and evolution: concepts, insights and challenges from a developmental model system. *Heredity (Edinb.)* **100**, 132–140 (2008).

37. Mouw, J. K. et al. Tissue mechanics modulate microRNA-dependent PTEN expression to regulate malignant progression. *Nat. Med.* **20**, 360–367 (2014).

38. Liu, G. et al. miR-21 mediates fibrogenic activation of pulmonary fibroblasts and lung fibrosis. *J. Exp. Med.* **207**, 1589–1597 (2010).

39. Cushing, L. et al. miR-29 is a major regulator of genes associated with pulmonary fibrosis. *Am. J. Respir. Cell Mol. Biol.* **45**, 287–294 (2011).

40. Herrera, J. et al. Dicer1 deficiency in the idiopathic pulmonary fibrosis fibroblastic focus promotes fibrosis by suppressing microRNA biogenesis. *Am. J. Respir. Crit. Care Med.* **198**, 486–496 (2018).

41. Parker, M. W. et al. Fibrotic extracellular matrix activates a profibrotic positive feedback loop. *J. Clin. Invest.* **124**, 1622–1635 (2014).

42. Pandit, K. V. & Milosevic, J. MicroRNA regulatory networks in idiopathic pulmonary fibrosis. *Biochem. Cell Biol.* **93**, 129–137 (2015).

43. Wynn, T. A. & Ramalingam, T. R. Mechanisms of fibrosis: therapeutic translation for fibrotic disease. *Nat. Med.* **18**, 1028–1040 (2012).

44. Liu, J. et al. Argonaute2 is the catalytic engine of mammalian RNAi. *Science* **305**, 1437–1441 (2004).

45. McCall, M. N. et al. MicroRNA profiling of diverse endothelial cell types. *BMC Med. Genomics* **4**, 78 (2011).

46. Krzywinski, M. et al. Circos: an information aesthetic for comparative genomics. *Genome Res.* **19**, 1639–1645 (2009).

Author contributions

S.N. and M.S. conceived the project. A.M. and T.D. performed the experiments, analysed the data and A.M. developed the computational data analysis. W.A. performed and analysed the zebrafish fin-fold regeneration experiments. L.C.B. performed and analysed the experiments in Supplementary Figs. 2b,c, 3b–d and 6. S.J.A. performed the cell culture experiments in Supplementary Fig. 3a. N.B. and C.J. performed the 3D cell culture experiments and analysed the data. D.L., M.Gu, J.Z. and M.Gerstein developed the sequence data processing and analysed (mapping and peak calling) the AGO2-HITS-CLIP experiment. V.M. and J.S. performed the mass spectrometry proteomic analysis. D.M.K. made the miRNA and RNA-seq libraries. A.M., T.D., M.S. and S.N. designed the experiments. M.S. and S.N. wrote the manuscript. All authors edited the manuscript.

Competing interests

The authors declare no competing interests.

Additional information

Supplementary information is available for this paper at https://doi.org/10.1038/s41556-019-0272-y.

Reprints and permissions information is available at www.nature.com/reprints.

Correspondence and requests for materials should be addressed to M.S. or S.N.

Publisher's note: Springer Nature remains neutral with regard to jurisdictional claims in published maps and institutional affiliations.

Methods

Cell culture. HUVECs and HUAECs were purchased from Cell Applications Inc. (catalogue no. 200-05n and catalogue no. 202-05n). Endothelial cells were cultured on dishes coated with 0.2% w/v gelatin (10 min at room temperature in PBS; Sigma) in endothelial cell growth medium (EGM Bullet Kit, Lonza). For HITS-CLIP assays, cells were used at P3 (split 1/3 and 1/5) before UV crosslinking. For other assays, cells were split 1:3 twice per week and used until passage 5. HDFs were purchased from the American Type Culture Collection (ATCC; catalogue no. PCS-201–010, lot no. 63014910) and cultured on 0.2% w/v gelatin-coated dishes in fibroblast growth medium (Fibroblast Growth Kit-Low Serum; PCS-201–041, ATCC). HDFs were split 1:10 twice per week and used until passage 6.

Primary fibroblasts. Primary dermal fibroblasts for 3D fibrin gel assays were obtained from 5 to 8-week-old C57BL/6 mice (Envigo). This study is compliant with all relevant ethical regulations regarding animal research. All procedures were in accordance with the UK Home Office regulation and UK animals (Scientific Procedures) Act of 1986 for the care and the use of animals. Mice were killed by a schedule 1 procedure by trained personnel. Mouse hair was removed and skin dissected in Hank's buffer supplemented with antibiotic and antimycotic solution (Sigma). Fat and excess connective tissues were removed, the dermis was minced with a scalpel and digested in buffer containing 0.25% trypsin without EDTA (Gibco), collagenase IV (4 mg ml^{-1} (Worthington) and calcium chloride (0.3 mg ml^{-1} (Sigma)) for 3 h at 37 °C with agitation during the last hour. After mechanical dissociation, cells were passed through a cell strainer (100 μm; Fischer Scientific). Cells were centrifuged at 1,800 r.p.m. for 5 min, resuspended in DMEM supplemented with 10% FBS (Sigma), penicillin (100 U ml^{-1}), streptomycin (100 μg ml^{-1}) (Gibco) and 1% ʟ-glutamine, and seeded in 75-cm^2 tissue culture flasks. Medium was changed at 3 h and subsequently changed once a day.

AGO2-HITS-CLIP. The HITS-CLIP experiment was performed as previously described[13]. Subconfluent endothelial cells in EGM were UV crosslinked two times with 400 mJ cm^{-2} in Stratalinker (model 2400, Stratagene), lysed and treated with DNase (1:1,000 Promega RQ1 DNase) and RNase T1 (1:100; Thermo Fisher). Cell lysates and Protein A Dynabeads (Invitrogen) complexed with Ab-panAGO-2A8 (MABE56, Millipore) were incubated at 4 °C for 4 h. Beads were subsequently washed and ligated with 3′-P32-radiolabelled linker (RL3; Supplementary Table 6). SDS–PAGE was performed using NuPage 4–12% Bis-Tris Gel (NP0321, Invitrogen), and proteins were transferred onto pure nitrocellulose membrane (BioTrace) using NuPAGE transfer buffer according to the manufacturer's instructions. High-performance autoradiography film was exposed overnight at −80 °C. The bands corresponding to AGO2-miRNAs (~110 kDa) and AGO2:RNA (~130 kDa) were cut and treated with proteinase K (Roche) to degrade proteins. RNAs were extracted and purified via phenol-chloroform, then a 5′-linker oligonucleotide (Supplementary Table 6) was ligated to the ends. cDNA libraries were generated using DNA oligos complementary to RL3 and SuperScriptIII reverse transcriptase (Invitrogen). Products were then PCR amplified using specific primers (DP5 and DP3; Supplementary Table 6) and purified via agarose PAGE 1% using a gel extraction kit (Qiagen). A second round of PCR was performed, using custom Illumina Hi-Seq primers with three different barcodes to multiplex the libraries (DSFP5, DSFP3-Index1, DSFP3-Index4 and DSFP3-Index8; Supplementary Table 6). Products were PAGE purified using the gel extraction kit, and libraries were analysed by the YCGA Sequencing Facility (New Haven, CT, USA) using a customized Illumina primer (SSP1; Supplementary Table 6).

HITS-CLIP data analysis. Prior to aligning sequencing reads, the raw data were analysed for quality steps to reduce artefacts: adapters were removed from raw reads, filtered according to quality scores and exact sequence duplicates were collapsed. Remaining reads were aligned using STAR RNA-seq aligner (version 2.4.1a)[47] using the UCSC hg19 reference human genome. A minimum of 10 bases matched was enforced, only unique reads were used and a maximum of 3 mismatches were allowed. Replicates were merged using SAMtools (version 1.2)[48] and the aligned reads were analysed with Piranha using a bin size of 30 bp. All identified peaks with $P < 0.05$ were mapped to Gencode version 22 annotation.

Conservation between artery and vein samples was calculated for each identified peak using PhastCons 100 conservation scores. Using Piranha peaks setting, a Wilcoxon rank sum test was performed to compare the difference in distribution of conservation score across samples.

For miRNA identification, reads were aligned using Novoalign (Novocraft; http://www.novocraft.com/products/novoalign/) against human miRNA sequences from miRBase (release 21)[49]. The miRNA expression levels were quantified as reads per million (RPM). Endothelial miRNAs identified in AGO2-HITS-CLIP were divided into families based on 8mer SEED regions.

Using TargetScan software[50], these miRNA SEED families were associated to the AGO2-HITS-CLIP peaks based on the putative MRE.

To test the expression of CAM versus other genes in cultured endothelial cells, we examined previously published microarray data performed in freshly isolated versus cultured HUVECs and HUAECs (Gene Expression Omnibus (GEO) ID: GSE43475)[51]. Standard microarray analysis for differential gene expression was performed using packages simplyaffy (http://bioinformatics.picr.man.ac.uk/simpleaffy/) and limma[52] from Bioconductor (http://www.bioconductor.org/).

CRISPR–Cas9 strategy to generate mutant primary cells. To mutate *AGO2* in HUVECs and HDFs, a pLentiCRISPR vector containing an AGO2 or a non-targeting gRNA (control, which does not target known mouse or human genome sequences) was used (Supplementary Table 6). Lentiviruses were generated by transfecting Lenti-X 293T cells (Clontech) with packaging vectors (2.5 μg VSV; 5 μg pxPAX2, Addgene) and the pLentiCRISPR DNA vector (7.5 ug) using Lipofectamine 2000 (Invitrogen). Virus containing supernatant was collected at 36 and 60 h post-transfection. Supplementary Fig. 2b shows a schematic of the approach. Cells were infected with the pLentiCRISPR virus containing AGO2 gRNAs or non-targeting gRNAs in the presence of polybrene (8 μg ml^{-1}). To generate cells with mutant MREs, similar vectors were generated to target the selected MRE sequences identified in the AGO2 HITS-CLIP experiment and confirmed via Sensor-seq. The complete lists of genes and gRNAs are reported in Supplementary Table 6. Cells were cultured for 7–10 d (up to a maximum of passage 5) prior to seeding on gels for immunostaining or traction force microscopy. Reduced AGO2 expression was confirmed by western blot at 7 and 10 d post-infection. Cells were lysed in RIPA buffer with protease and phosphatase inhibitor cocktail (Roche) on ice. Samples were loaded onto 8% or 4–12% SDS–PAGE gels, transferred on a Immun-Blot PVDF membrane (Bio-Rad), blocked with 10% milk for 2 h and incubated with rabbit anti-AGO2 (1:2,000; Cell Signaling) and mouse anti-β-ACTIN (Santa Cruz) overnight at 4 °C. Secondary antibody incubation was done with anti-mouse-horseradish peroxidase (HRP) and anti-rabbit-HRP (1:4,000; Santa Cruz) for 1 h. For blots of other proteins following MRE mutation, target protector or knockdown, membranes were blocked with 5% w/v BSA in PBS 0.1% Tween for 1 h and incubated with primary antibody for RHOB (1:200; sc-8048, Santa Cruz), CTGF (1:1,000; ab6992, Abcam), VINCULIN (1:2,500; V9131, Sigma-Aldrich), STMN1 (1:10,000; ab52630, Abcam), DROSHA (1:5,000; ab183732, Abcam) or GAPDH (1:4,000; 2118, Cell Signaling) overnight at 4 °C. After washing, membranes were incubated with secondary antibody anti-rabbit-HRP or anti-mouse-HRP (1:4,000; 7076P2 and 7074S, Cell Signaling) for 1 h at room temperature in 5% BSA TBST. After washing, blots were developed with super signal west pico chemiluminescent substrate (Thermo) using a SYNGENE G-Box imager.

Single amplicons of ~300 bp were generated using primes equidistant from the putative region of mutation. PCR amplicons were combined and sent to YGCA Sequencing Facility for MiSeq 2×250 analysis. After sequencing, single amplicons were demultiplexed and single reads were used for multiple sequence alignment (msa) against the WT sequence using the R msa package[53]. The frequency of each mutation was calculated as total reads for each CAM gene mutation divided by the sum of all of the reads aligned to a specific CAM gene, and plot as a bar plot.

To mutate *Ago2* in mouse fibroblasts, pLentiCRISPRV2 (Addgene) vectors containing Ago2 or non-targeting gRNAs (control, as above) were used. P0 fibroblasts at 80% confluence were infected with lentivirus containing either non-targeting or Ago2 gRNA in the presence of 4 mg ml^{-1} polybrene for 16 h. Culture medium was changed and cells were incubated for 72 h. Infected cells were selected in medium with 0.5 ug ml^{-1} puromycin for 48 h (this concentration efficiently kills all control cells) and then cultured for another 96 h before use in matrix constructs. Reduced Ago2 expression in mouse fibroblast constructs was confirmed by western blot at 5 d. Matrix constructs were washed with cold PBS, frozen in liquid nitrogen, then homogenized with metallic beads in a Bullet Blender (Strom 24, Next Advance) in protein extraction buffer (1.1% sodium dodecyl sulphate, 0.3% sodium deoxycholate, 25 mM dithiothretol, in 25 mM ammonium bicarbonate with complete anti-protease and anti-phosphatase; Roche). Protein samples were loaded in a 4–12% Nu-Page pre-casted gel (Thermo Scientific) for electrophoresis (200 V for 50 min), transferred to nitrocellulose membrane (Bio-Rad), blocked for 1 h with Odyssey PBS blocking buffer (LI-COR Biosciences) and incubated overnight with antibodies against Ago2 (1:2,000; Cell Signaling) and β-actin (1:5,000; Abcam). After washing in PBS-Tween, membranes were incubated with Alexa Fluor-680 anti-mouse and Alexa Fluor-800 anti-rabbit (both from Thermo, 1:15,000). Membranes were scanned with an Odyssey CLX NIR scanner (LI-COR Biosciences) and fluorescence intensity of the bands quantified with the Image Studio software (LI-COR Biosciences).

shRNA knockdown of DROSHA and miRNA target protector for CTGF. Knockdown of DROSHA was performed using Dharmacon shRNA SMARTvectors (GE Healthcare). Lentivirus was prepared in Lenti-X 293T cells as before using a non-targeting negative control short hairpin RNA (shRNA) and two shRNAs directed at DROSHA (negative control shRNA, shDRO#1 and shDRO#2; Supplementary Table 6). Experiments were performed with shDRO#2 (~95% knockdown at 5 d). DROSHA knockdown was verified by immunoblot as before with DROSHA antibody (1:5,000; ab183732, Abcam).

Disruption of the miRNA–MRE interaction with the *CTGF* gene was performed using a miScript Target Protector (Qiagen) directed at the MRE within the human *CTGF* gene. The CTGF target protector (CTGF_1_TP, catalogue no. MTP0079186) or the negative control target protector (catalogue no. MTP0000002) were transfected into P2 HUVECs at 20 nM using Lipofectamine

RNAiMax (Invitrogen) in OPTI-MEM (Gibco) with 4% FBS (Sigma) twice (1 and 3 d post-seeding). CTGF expression increases post-transfection were verified by immunoblot as before with a CTGF antibody (1:1000; ab6992, Abcam).

Polydimethylsiloxane and polyacrylamide substrates. Polydimethylsiloxane (PDMS) substrates were cast in the bottom of 10-cm tissue culture dishes or #1.5 cover-glass bottomed 35-mm Mattek dishes (for imaging studies). Soft (3 kPa) gels were made using a 1/1 ratio (by weight) of PDMS components A and B (CY 52–276 A and B, Dow Corning), degassed for 30 min in a vacuum desiccator and cured for 24 h at room temperature. Stiff (30 kPa) gels were made using a 40/1 ratio (by weight) of SYLGARD 184 components B and C (SYLGARD 184, Dow Corning), degassed for 30 min and cured for 3 h at 70 °C. Prior to seeding, gels were washed with PBS, sterilized with UV for 20 min and coated with bovine plasma fibronectin (10 µg ml^{-1} in PBS) overnight at 4 °C.

Polyacrylamide gels were prepared using a protocol modified from previously published methods[54]. Briefly, 30-mm glass bottom dishes were activated with glacial acetic acid, 3-(trimethoxysilyl) propyl methacrylate and 96% ethanol solution (1/1/14 ratio, respectively) for 10 min at room temperature. For fibronectin protein conjugation (1 mg ml^{-1}) on the polyacrylamide gel, acrylic acid N-hydroxysuccinimide ester was partially mixed as a substitute of acrylamide. Each stiffness was prepared with the ratio shown in Supplementary Table 9, which was previously reported[54].

RNA, miRNA and Sensor-seq library preparation. Total RNA was extracted from three replicates of cultured HUVEC or HDF cells seeded on 3 kPa or 30 kPa PDMS using TRIzol reagent (Life Technologies) according to the manufacturer's protocol. For mRNA libraries, total RNA was treated with DNA-free DNase (Ambion) and 500 ng of treated RNA was used to prepare Lexogen QuantSeq 3′ mRNA-Seq FWD libraries for Illumina deep-sequencing according to the manufacturer's protocols. Libraries were amplified with 12 PCR cycles. miRNA libraries were prepared from 1 µg of total RNA using the NEBNext Small RNA Library Kit (NEB) following the gel size selection method in the manufacturer's protocol and submitted for Illumina sequencing. For the Sensor-seq library, a customized oligonucleotide library was synthetized by Integrated DNA Technologies. The sequence of each individual oligonucleotide was obtained from Piranha analysis (see Supplementary Table 4), extending the genomic coordinate of each peak by 20 nt at the 3′ and 5′ regions. Ninety-seven peaks with at least 1 predicted MRE, representing 51 CAM genes, were selected. In addition, all sensor oligonucleotides contained restriction enzyme sites, AscI and NheI, allowing for PCR base amplification and cloning. The oligonucleotide library was resuspended in 480 µl of water, diluted 1:100 and PCR amplified using the Phusion HotStart II HF kit and AscI forward and NheI reverse primers (Supplementary Table 6). PCR-amplified libraries were purified using a PCR purification kit (Qiagen) and double digested for 2 h at 37 °C.

Sensor-seq backbone[18] containing a bidirectional promoter for *UbC* upstream of the genes encoding copGFP and mCherry, was kindly provided by J. Lu, Yale University. After sensor backbone digestion with AscI and NheI, the MRE oligo library was cloned into the 3′ UTR of mCherry. Ligation using T4 DNA ligase (Promega) was incubated for 16 h at 16 °C, then transformed into DH5-α, and pooled colonies were used to prepare a library Maxi prep (Qiagen).

Lentiviruses for the expression of the CAM MRE sensor library were generated as above using Lenti-X 293T cells. For FACS analysis, additional control lentiviruses expressing GFP alone, mCherry alone, miRNA sensor lacking a MRE (empty sensor plasmid, negative control) and miRNA sensor with a synthetic MRE for miR-125 (miR-125 sensor plasmid, positive control) were used.

RNA-seq and miRNA-seq data analysis. Total RNA and miRNA were aligned against the human genome version GRCh38 using the GENCODE 22 transcript annotation, using STAR alignment software with the same parameters used for the ENDOCE project (www.encodeproject.org).

After alignment, differential gene expression of RNAs or miRNAs between endothelial cells seeded on 30- and 3-kPa substrates was computed using the negative binomial distributions via edgeR using standard parameter Genes[55,56]. The levels (log$_2$ fold change) of CAM RNAs and SEED matching miRNAs to CAM MRE sensors were combined and represented in the CIRCOS plot.

FACS and Sensor-seq analysis. For FACS experiments, cells were infected with low levels of the library or control lentivirus in the absence of polybrene to avoid multiply infected cells (10–20% of cells infected). After 48 h, cells were trypsinized and seeded onto soft (3 kPa) or stiff (30 kPa) fibronectin-coated PDMS dishes at low density (150,000 cells per 10-cm dish) for 2 d. Cells were then washed once with PBS, trypsinized, centrifuged for 5 min at 300g and resuspended in PBS at 500,000 cells per ml immediately before FACS analysis. Infected cells were sorted on a BD FACSAria II and analysed with FACSDiva 7. Four sorting gates were set based on the two control plasmids (empty sensor and miR-125 sensor). The upper limit bin (not suppressed) was designed to contain 90% or more events per cells infected with the empty sensor and less than 0.5% of events for the miR-125 sensor. Conversely, the lower two bins (strongly suppressed and suppressed) were designed to contain 90% of events coming from cells infected with the miR-125 sensor, in a ratio close to 3/2 (~60% of events in the strongly suppressed bin and

~40% of events in the suppressed bin). The third bin (mildly suppressed) was set between the not suppressed and the suppressed bins. For clarity, the contour plot represents the total percentage of event in each single bins, grouped in a 'island' of 15% probability were shown for the empty sensor, miR-125 sensor, sensor library at 3 kPa and sensor library at 30 kPa.

After sorting of cells into each bin, genomic DNA was isolated using the DNeasy Blood and Tissue Kit (Qiagen) and the MREs were PCR amplified using specific forward primers to barcode each bin (strongly suppressed, suppressed, mildly suppressed, not suppressed and a reverse primer; Supplementary Table 6). PCR was performed using Phusion HotStart II HF with a melting temperature of 59 °C for 20 s. The libraries were purified using a gel extraction kit (Qiagen). The primers used contain barcodes for multiplexing and were designed to hybridize with Illumina sequencing.

Computational analysis of Sensor-seq was performed using R. First, the number of reads for each sensor MRE was divided by the total number of reads in the entire experiment and multiplied by 1 million to get the RPM for each sensor. To calculate the frequency of sensor MREs in each bin, the RPM was divided by the total RPM for all four bins of the experiment for that sensor, giving frequency values for each MRE in each bin at each stiffness. MREs that showed a dominant bin (with frequency values above 0.375, that is, non-random) were compared at 3 kPa versus 30 kPa. In Fig. 2c, CAM MREs were then plotted based on the reproducible tendency to be enriched in the same bin at a given stiffness but not the other for three independent experiments. MREs that shifted towards a more suppressed bin on 30 kPa than on 3 kPa were plotted as CAM MRE 30 kPa (bottom left of plot). MREs that shifted towards a more suppressed bin on 3 kPa than on 30 kPa were plotted as CAM MRE 3 kPa (upper right of plot). RNA-seq (red) and proteomics (green) data for each of these proteins were plotted and linked with the miRNA-seq (for miRNAs predicted to bind to these MREs). The regulation of CAM MREs by miRNAs (stars, Fig. 2c) was further validated by individual MRE mutagenesis followed by functional assays.

Mass spectrometry sample preparation and analysis. Cell pellets were lysed in 50 µl of 25 mM ammonium bicarbonate (Fluka) buffer containing 1.1% SDS (Sigma), 0.3% sodium deoxycholate (Sigma), protease inhibitor cocktail (Sigma) and phosphatase inhibitor cocktail (Merck). Six 1.6-mm steel beads (Next Advance) were added and samples were homogenized with a Bullet Blender (Next Advance) at maximum speed for 2 min. Homogenates were subjected to centrifugation (12 °C at 10,000 r.p.m. for 5 min). Lysates were added to 150 µl digest buffer (1.33 mM CaCl$_2$Sigma) in 25 mM ammonium bicarbonate) containing immobilized trypsin beads (Perfinity Biosciences) and shaken at 1,400 r.p.m. overnight at 37 °C. The resulting digests were reduced with 4 µl of 500 mM dithiothreitol (Sigma; in 25 mM ammonium bicarbonate; for 10 min shaking at 1,400 r.p.m. at 60 °C) and alkylated with 12 µl of 500 mM iodoacetamide (Sigma; in 25 mM ammonium bicarbonate; for 30 min shaking, in the dark, at room temperature). Trypsin beads were removed by centrifugation (10,000 r.p.m. for 10 min). Supernatant were transferred to 1.5 ml 'LoBind' Eppendorf tubes and acidified with 5 µl 10% trifluoroacetic acid (Riedel-de Haën) in water and cleaned by two-phase extraction (3× addition of 200 µl ethyl acetate (Sigma), followed by vortexing and aspiration of the organic layer). Peptides were desalted with POROS R3 beads (Thermo Fisher) using the manufacturer's protocol and lyophilized. Peptide concentrations were measured by spectrophotometer (Direct Detect, Millipore) and adjusted to 200 ng µl^{-1} in injection buffer (5% HPLC grade acetonitrile and 0.1 % trifluoroacetic acid in deionized water (Fisher Scientific)). LC–MS/MS was performed using an UltiMate 3000 Rapid Separation liquid chromatography system (RSLC, Dionex Corporation) coupled to a Q Exactive HF mass spectrometer (Thermo Fisher). Peptides were separated using a multistep gradient from 95% A (0.1% formic acid in water (Fisher Scientific)) and 5% B (0.1% formic acid in acetonitrile) to 7% B at 1 min, 18% B at 58 min, 27% B at 72 min and 60% B at 74 min at 300 nl min^{-1}, using a 75 mm × 250 µm inner diameter 1.7-µM CSH C18, analytical column (Waters). Peptides were selected for fragmentation automatically by data-dependent analysis.

Mass spectrometry data processing and protein quantification. All sample spectra were aligned using Progenesis QI (Nonlinear Dynamics) with manual placement of vectors where necessary. Default parameters were used except where noted. Peak-picking sensitivity was set to 4/5. Peptides with charges between +1 and +4, with 2 or more isotopes, were selected for analysis. Peptide identities were assigned using Mascot (Matrix Science), searching against the SwissProt and TREMBL mouse databases. The database was modified to search for cysteine alkylation (monoisotopic mass change: 57.021 Da), oxidized methionine (15.995 Da), hydroxylation of asparagine, aspartic acid, proline or lysine (15.995 Da) and phosphorylation of serine, tyrosine or threonine (79.966 Da). A maximum of two missed cleavages was allowed. Peptide intensities were exported as Excel (Microsoft) spreadsheets for processing with MATLAB (The MathWorks). Peptide identifications were filtered via Mascot scores, selecting only those with a Benjamini–Hochberg false discovery rate of <0.05. Raw ion intensities from peptides belonging to proteins with fewer than two unique (by sequence) peptides per protein in the data set were excluded from quantification. Peptides from CAM proteins were only used for quantification if they were unique to the protein (that

is, they did not overlap with other protein sequences). Intensities were logged and normalized by the median logged intensity. Missing values were assumed as missing due to low abundance, as described[57]. Imputation was performed at the peptide level using a method similar to Perseus[58], whereby missing values were imputed randomly from a normal distribution centred on the apparent limit of detection for the experiment. The limit of detection was determined by taking the mean of all minimum logged intensities and downshifting it by 1.6σ, where σ is the standard deviation of the minimum logged peptide intensities. The width of this normal distribution was set to 0.3σ as described in ref. [58]. Fold-change differences in protein quantities were calculated by fitting a mixed-effects linear regression model for each protein with Huber weighting of residuals as described in ref. [57] using the fitglme function (MATLAB) with the formula:

$$y_{ipt} = \beta_0 + X_p\beta_p + X_t\beta_t + \varepsilon_{ipt}$$

where y_{ipt} represents the log$_2$ (intensity) of peptide p belonging to protein i, under experimental treatment t. β represents the effect sizes for the indicated coefficients. Peptide effects were considered as random effects, whereas treatment was considered as a fixed effect. β_0 denotes the intercept term and ε_{ipt} denotes residual variance. Standard error estimates were adjusted with empirical Bayes variance correction according to ref. [59]. Conditions were compared with two-sided empirical Bayes-adjusted t-tests with Benjamini–Hochberg correction for false positives.

Cell immunostaining and quantification. Cells seeded on fibronectin-coated PDMS were fixed with 4% paraformaldehyde (Electron Microscopy Sciences) in PBS. Cells were then washed and permeabilized with 0.05% Triton X-100 in PBS, with 320 mM sucrose and 6 mM MgCl$_2$. Cells were PBS washed 3 times, blocked for 30 min with 1% BSA in PBS, then incubated overnight at 4 °C with anti-YAP antibody (1:200; sc-101199, Santa Cruz Biotechnology), anti-RHOB (1:250; 19HCLC, Thermo Fisher), anti-VINCULIN (1:200; V9131, Sigma-Aldrich), anti-STMN1 (1:200; ab52630, Abcam), anti-CTGF (1:200; ab6992, Abcam) and anti-PAXILLIN (1:800, RabMAb Y113; ab32084, Abcam) diluted in 1% BSA in PBS. Cells were washed 3 times with PBS and incubated at room temperature for 1 h with secondary antibodies (Alexa-488 anti-rabbit, Alexa-647 anti-mouse, 1:1,000; Thermo Fisher) and Alexa-565-conjugated phalloidin (1:1,000; Molecular Probes). Cells were washed three times with PBS and mounted with 4,6-diamidino-2-phenylindole (DAPI) in Fluoromount-G (SouthernBiotech). Cell areas were quantified using ImageJ by background subtracting, thresholding to generate cell masks and using the analyse particles function. YAP staining was quantified by taking the average nuclear YAP signal (in the area of the DAPI stain), divided by the average cytoplasmic YAP signal (in the area of the non-nuclear cell mask). Focal adhesions were analysed using the Focal Adhesion Analysis Server[60] with the minimum adhesion size set to 0.5 µm^2 and the default settings for only static properties. The average number of focal adhesions per cell was calculated for each field of view by dividing the total number of adhesions in the field by the number of cells.

Traction force microscopy. PDMS traction force microscopy substrates were fabricated as described[61]. Briefly, cover-glass bottom dishes were spin coated to obtain a ~40-µm thick layer of PDMS (SYLGARD 184 by Down Corning mixed at various B/C ratios, 67/1 for 3 kPa and 40/1 for 30 kPa) and cured at 70 °C for 3 h. Gels were then treated with 3-aminopropyl trimethoxysilane for 5 min and incubated for 10 min at room temperature with 40-nm Alexa Fluor-647 beads (Molecular Probes) suspended in a 100 µg ml^{-1} solution of 1-ethyl-3-(3-dimethylaminopropyl) carbodiimide (Sigma) in water to covalently link the beads to the gel surface. Elastic moduli were measured using an Instron 5848 (Supplementary Fig. 2a) and reported as the Young's modulus (E).

Traction force microscopy gels were coated with fibronectin (10 µg ml^{-1}) in PBS overnight at 4 °C and washed 3 times with PBS. HUVECs and HDFs were seeded on the gels in EGM or low serum fibroblast growth medium, respectively, 24 h before analysis at low density (~3,000 cells per cm^2). Cells and florescent beads were imaged on a spinning-disk confocal microscope (UltraVIEW VoX, Perkins Elmer) attached to a Nikon A-1 microscope equipped with a temperature- and CO$_2$-controlled incubation chamber and ×60 1.4 NA lens. Fluorescent images of Alexa Fluor-647 beads and differential interference contrast images of cells were acquired before and after cell lysis with 0.05% SDS. Images were drift corrected and bead displacements were quantified as described[62]. Force fields and traction stresses were calculated using FTTC (Fourier transform traction cytometry) force reconstruction with the regularization parameter set to 0.007. The total force per cell was calculated as the average stress under the cell multiplied by the area.

3D matrix constructs. A method to generate 3D cell-derived uniaxial matrix constructs (3D matrix constructs) based on the 'tendon construct' developed by K. Kadler's group was used[63]. Six-well plates were coated with a 2-mm layer of SYLGARD 184 and incubated overnight at 65 °C to induce polymerization. After cooling, the (hydrophobic) SYLGARD layer was incubated for 15 min with Pluronic F-127. Custom-made rectangular Teflon molds (15 × 10 × 2 mm) were sterilized with Virkon (10 min) and then ethanol 70% (15 min). Inside the molds, two 8-mm segments of size 0 silk sutures were pinned to the PDMS using

insect pins exactly 10 mm apart. Inside each mold, we added 12 µl thrombin stock solution (200 U ml^{-1}; Sigma). Primary fibroblasts were detached with 0.05% trypsin, centrifuged at 1,800 r.p.m. and counted. For each matrix construct, 2 × 10^5 cells were resuspended in 300 µl DMEM containing 8 mg ml^{-1} fibrinogen (Sigma) and 0.2 mM L-ascorbate-2-phosphate. Cell suspensions were injected inside the molds and placed at 37 °C for 15 min in the incubator for polymerization. After polymerization, the Teflon mold was removed and one additional insect pin was added to maintain the suture thread. Matrix constructs were cultured with DMEM/F12 supplemented with 10% FBS (Sigma), penicillin (100 U ml^{-1}), streptomycin (100 µg ml^{-1}; Gibco), 1% L-glutamine and 0.2 mM L-ascorbate-2-phosphate. The 3D matrix constructs were cultured for 5 d and the culture medium was changed every other day. After 5 d, photographs of the constructs were taken with a Nikon reflex camera equipped with a 50-mm macro-objective at a focal distance of 1:1. The diameter of constructs was obtained by averaging the diameter at three different locations (each extremity and the middle).

Immunostaining matrix constructs. Matrix constructs were rinsed in cold PBS and fixed overnight at 4 °C in 4% formaldehyde (Pierce 16% formaldehyde, methanol free) in PBS. Fixation constructs were dehydrated, embedded in paraffin and 5-µm transverse sections cut with a Leica microtome. For immunostaining, we performed a rehydration protocol followed by antigen retrieval for 30 min at 96 °C in a citrate buffer (pH 6). Sections were blocked with Odyssey PBS blocking buffer (LI-COR Biosciences) for 1 h and incubated overnight with primary antibodies diluted in blocking buffer: vimentin (1:400; Cell Signaling) and phospho-myosin light chain (1:400; Abcam). After extensive rinsing in PBS Tween 0.1%, slides were incubated with Alexa Fluor-647 anti-rabbit secondary antibody (1:500; Thermo Scientific) for 1 h at room temperature, thoroughly washed with PBS Tween 0.1% and slides were mounted in Fluoromount-G-DAPI (SouthernBiotech). Slides were imaged with an Olympus slide scanner microscope equipped with a ×20 objective.

Zebrafish fin-fold regeneration. This study is compliant with all relevant ethical regulations regarding animal research. Zebrafish were raised and maintained at 28.5 °C using standard methods and according to protocols approved by Yale University Institutional Animal Care and Use Committee (IACUC no. 2017-11473). WT (AB) and mz ago2$^{-/-}$ mutants[28] were used. To generate the ctgfa MRE mutant, zebrafish AB were injected with 125 ng µl^{-1} Cas9 mRNA and 75 ng µl^{-1} gRNAs, designed as previously described[64]. The gRNA sequence used to target the conserved MRE within the 3′ UTR human CTGF gene was (CTGF MRE gRNA; Supplementary Table 6). Genomic DNA was isolated from a clutch of 15 injected and uninjected control embryos at 24 h post-fertilization (h.p.f.) using the Qiagen DNeasy Blood and Tissue Kit. Genomic DNA (250 ng) and the Phusion HotStart II Kit (Thermo Fisher) used to PCR amplify an approximately 300-bp region surrounding the intended MRE target (MRE Fw Amp, MRE Rv Amp; Supplementary Table 6). The T7 endonuclease I assay was used to detect mutations as described in the manufacturer's protocol (New England BioLabs). PCR and T7 products were run on 3% agarose gels to verify the occurrence of insertions and deletions in the MRE sequence. The remaining embryos were grown to 48 h.p.f. and used for the fin-fold regeneration experiments (see below).

The zebrafish miR-124 sensor assay and ctgfa mRNA injection were performed as described[64]. For the fin-fold regeneration assay, we used 14 AB fish, 14 mz ago2$^{-/-}$ mutant embryos and 15 mz ago2$^{-/-}$ fish injected at the 1cell stage with 200 pg of in vitro-transcribed mRNA encoding the human AGO2 protein. At 2 d post-fertilization, the fin fold was cut at the edge of the fin using a 25-G needle. Bright-field images were captured at 0.5, 2, 4, 24, 48 and 72 h.p.a. using a Leica M165 FC stereomicroscope and Leica Application Suite V4 software. The length of the fins over time was measured using FIJI-ImageJ[65,66] and normalized for the length of the fin before cutting.

Zebrafish immunofluorescence assay. For the fluorescent images: 20 embryos for each genotype (AB, Ago2 mutant (−/−) and Ctgfa 3′ UTR mutant) were cut and then at 0.5, 2, 4 and 24 h.p.a. were fixed in 4% paraformaldehyde overnight at 4 °C. Embryos were washed 4–5 times with PBS 0.1% Tween, then incubated 2 h in blocking solution (0.8% Triton X-100, 10% normal goat serum, 1% BSA and 0.01% sodium azide in PBS Tween). Zebrafish were stained following the protocol as in ref. [12] using the primary antibody mouse anti-phospho-myosin light chain 2 (1:200; Cell Signaling), mouse anti-proliferating cell nuclear antigen (1:200; Dako), rabbit anti-fibronectin (1:200; Sigma), DAPI (1:1,000; Sigma), rabbit anti-CTGFA (1:150; Abcam) and mouse anti-YAP (1:200; Santa Cruz Biotechnology), and the secondary antibody Alexa Fluor-488 anti-mouse (1:250, Thermo Fisher) and Alexa Fluor-596 anti-rabbit (1:250, Thermo Fisher). After staining, images were captured using a Leica Microsystems SP5 confocal microscope using a ×40 objective. Max projections were generated and intensity was quantified using FIJI-Image. For each protein staining, the intensity profile of 4–6 fish was calculated for a section of 80 µm in diameter within the wound and 50 µm from the fin-fold edge. The ratio of nuclear-to-cytosolic YAP was calculated before and during the fin-fold regeneration from confocal images thresholded using the DAPI channel to generate a binary mask for the nuclei. Using ImageJ, the binary mask was used to generate a nuclear and a cytosolic YAP image. Each was ratioed and normalized to the area. For the TUNEL assay, to detect apoptotic cells, embryos were fixed

in 4% paraformaldehyde overnight and stored in 100% methanol at −20 °C. The TUNEL assay was performed using the ApopTag Red In Situ Apoptosis Detection Kit (Millipore).

AFM. Live zebrafish embryos (48 h.p.f.) were anaesthetized using 1× tricaine in egg water and mounted on PDMS gels. The tips of fish tails were probed using a DNP-10 D tip (Bruker; nominal stiffness ~0.06 N m⁻¹) on a Bruker Dimension FastScan AFM immersed in egg water containing 1× tricaine. Probe deflection sensitivity was calibrated by taking indentation curves on glass, and the nominal tip stiffness was calibrated by thermal tuning (assuming a simple harmonic oscillator in water). Force versus deflection curves were collected for a ramp size of 1.5 µm at a rate of 750 nm s⁻¹ for at least 2 locations per fish, with 10–11 fish measured per group. The first 600 nm of the extension curves were fit with NanoScope Analysis Software version 1.5 (Bruker) assuming a Poisson's ratio of 0.5 and using the Sneddon fit model[67].

Statistics and reproducibility. All of the statistical analysis were performed using Prism version 7.01 (GraphPad) and R, except for the peak identification, which used Piranha software[68] to measure the significance of read coverage height for each mapped position using the zero-truncated negative binomial model. To confirm changes in cell area, focal adhesion number, YAP localization and traction force generation, t-tests were performed using Prism to assess the change in the mean between WT and AGO2 or MRE CRISPR–Cas9 mutant cells. These data sets contained more than 20 individual measurements for each condition and showed a log-normal distribution. For in vivo analysis of zebrafish WT and Ago2 mutants, changes in fin-fold tissue were analysed using t-tests; fin-fold regeneration was analysed via two-way analysis of variance (ANOVA) and Sidak's multiple comparisons test for 4–6 individual fish for a data set using Prism. Figure legends indicate the exact number of measurements, the number of independent experiments and the statistical test used for each analysis performed.

Reporting Summary. Further information on research design is available in the Nature Research Reporting Summary linked to this article.

Data availability

RNA-seq and small RNA-seq data for endothelial cells that support the findings of this study have been deposited in the GEO under accession codes GSE99686 and GSE11021. Small RNA-seq data for HDF have been deposited in the GEO under accession code GSE123008. HITS-CLIP data have been deposited in the Sequence Read Archive (SRA) under accession code PRJNA507245. Proteomics data have been uploaded to the PRIDE depository (PXD011882) and results are summarized in Supplementary Table 5. Source data for all figures and supplementary figures have been provided as Supplementary Table 8.

References

47. Dobin, A. et al. STAR: ultrafast universal RNA-seq aligner. *Bioinformatics* **29**, 15–21 (2013).
48. Li, H. et al. The Sequence Alignment/Map format and SAMtools. *Bioinformatics* **25**, 2078–2079 (2009).
49. Kozomara, A. & Griffiths-Jones, S. miRBase: annotating high confidence microRNAs using deep sequencing data. *Nucleic Acids Res.* **42**, D68–D73 (2014).
50. Agarwal, V., Bell, G. W., Nam, J. W. & Bartel, D. P. Predicting effective microRNA target sites in mammalian mRNAs. *eLife* **4**, e05005 (2015).
51. Aranguren, X. L. et al. Unraveling a novel transcription factor code determining the human arterial-specific endothelial cell signature. *Blood* **122**, 3982–3992 (2013).
52. Ritchie, M. E. et al. limma powers differential expression analyses for RNA-sequencing and microarray studies. *Nucleic Acids Res.* **43**, e47 (2015).
53. Bodenhofer, U., Bonatesta, E., Horejs-Kainrath, C. & Hochreiter, S. msa: an R package for multiple sequence alignment. *Bioinformatics* **31**, 3997–3999 (2015).
54. Elosegui-Artola, A. et al. Mechanical regulation of a molecular clutch defines force transmission and transduction in response to matrix rigidity. *Nat. Cell Biol.* **18**, 540–548 (2016).
55. Robinson, M. D., McCarthy, D. J. & Smyth, G. K. edgeR: a Bioconductor package for differential expression analysis of digital gene expression data. *Bioinformatics* **26**, 139–140 (2010).
56. McCarthy, D. J., Chen, Y. & Smyth, G. K. Differential expression analysis of multifactor RNA-seq experiments with respect to biological variation. *Nucleic Acids Res.* **40**, 4288–4297 (2012).
57. Goeminne, L. J., Gevaert, K. & Clement, L. Peptide-level robust ridge regression improves estimation, sensitivity, and specificity in data-dependent quantitative label-free shotgun proteomics. *Mol. Cell. Proteomics* **15**, 657–668 (2016).
58. Tyanova, S. et al. The Perseus computational platform for comprehensive analysis of (prote)omics data. *Nat. Methods* **13**, 731–740 (2016).
59. Smyth, G. K. Linear models and empirical Bayes methods for assessing differential expression in microarray experiments. *Stat. Appl. Genet. Mol. Biol.* **3**, Article3 (2004).
60. Berginski, M. E. & Gomez, S. M. The Focal Adhesion Analysis Server: a web tool for analyzing focal adhesion dynamics. *F1000Res.* **2**, 68 (2013).
61. Gutierrez, E. & Groisman, A. Measurements of elastic moduli of silicone gel substrates with a microfluidic device. *PLoS ONE* **6**, e25534 (2011).
62. Han, S. J., Oak, Y., Groisman, A. & Danuser, G. Traction microscopy to identify force modulation in subresolution adhesions. *Nat. Methods* **12**, 653–656 (2015).
63. Kapacee, Z. et al. Tension is required for fibripositor formation. *Matrix Biol.* **27**, 371–375 (2008).
64. Narayanan, A. et al. In vivo mutagenesis of miRNA gene families using a scalable multiplexed CRISPR/Cas9 nuclease system. *Sci. Rep.* **6**, 32386 (2016).
65. Schindelin, J. et al. Fiji: an open-source platform for biological-image analysis. *Nat. Methods* **9**, 676–682 (2012).
66. Le Guyader, D. et al. Origins and unconventional behavior of neutrophils in developing zebrafish. *Blood* **111**, 132–141 (2008).
67. Sneddon, I. N. The relation between load and penetration in the axisymmetric boussinesq problem for a punch of arbitrary profile. *Int. J. Eng. Sci.* **3**, 47–57 (1965).
68. Uren, P. J. et al. Site identification in high-throughput RNA–protein interaction data. *Bioinformatics* **28**, 3013–3020 (2012).

nature research

Corresponding author(s):   Martin Schwarz and Stefania Nicoli

Reporting Summary

Nature Research wishes to improve the reproducibility of the work that we publish. This form provides structure for consistency and transparency in reporting. For further information on Nature Research policies, see Authors & Referees and the Editorial Policy Checklist.

Statistical parameters

When statistical analyses are reported, confirm that the following items are present in the relevant location (e.g. figure legend, table legend, main text, or Methods section).

n/a	Confirmed	
☐	☒	The exact sample size (*n*) for each experimental group/condition, given as a discrete number and unit of measurement
☐	☒	An indication of whether measurements were taken from distinct samples or whether the same sample was measured repeatedly
☐	☒	The statistical test(s) used AND whether they are one- or two-sided *Only common tests should be described solely by name; describe more complex techniques in the Methods section.*
☐	☒	A description of all covariates tested
☐	☒	A description of any assumptions or corrections, such as tests of normality and adjustment for multiple comparisons
☐	☒	A full description of the statistics including central tendency (e.g. means) or other basic estimates (e.g. regression coefficient) AND variation (e.g. standard deviation) or associated estimates of uncertainty (e.g. confidence intervals)
☐	☒	For null hypothesis testing, the test statistic (e.g. *F*, *t*, *r*) with confidence intervals, effect sizes, degrees of freedom and *P* value noted *Give P values as exact values whenever suitable.*
☒	☐	For Bayesian analysis, information on the choice of priors and Markov chain Monte Carlo settings
☒	☐	For hierarchical and complex designs, identification of the appropriate level for tests and full reporting of outcomes
☒	☐	Estimates of effect sizes (e.g. Cohen's *d*, Pearson's *r*), indicating how they were calculated
☐	☒	Clearly defined error bars *State explicitly what error bars represent (e.g. SD, SE, CI)*

Our web collection on statistics for biologists may be useful.

Software and code

Policy information about availability of computer code

Data collection	Volocity (PerkinElmer) v6.3.1 BD FACSDiva 7 Bruker NanoScope v1.5 (AFM)
Data analysis	ImageJ v1.6.0 (masking cells) Matlab v R2015a (TFM) TFM software (open source, available from the Danuser lab website: https://www.utsouthwestern.edu/labs/danuser/software/) Graphpad Prism v 7.01 (statistical analysis) Bruker NanoScope Analysis v1.5 (AFM) R and Rstudio v 3.3.3 and v 1.0.143 (statistical analysis) Samtools (version 1.2) Gencode (version 22) Novoalign miRBase (release 21) TargetScan Bioconductor Library with simplyaffy and limma packages Progenesis QI (Nonlinear Dynamics) Mascot (Matrix Science UK) with Swiss Prot and TREMBL mouse databases

For manuscripts utilizing custom algorithms or software that are central to the research but not yet described in published literature, software must be made available to editors/reviewers upon request. We strongly encourage code deposition in a community repository (e.g. GitHub). See the Nature Research guidelines for submitting code & software for further information.

Data

Policy information about availability of data

All manuscripts must include a data availability statement. This statement should provide the following information, where applicable:
- Accession codes, unique identifiers, or web links for publicly available datasets
- A list of figures that have associated raw data
- A description of any restrictions on data availability

The accession number for all the sequence reads reported in this paper are:
HITS-CLIP in Sequence Read Archive (SRA) under accession code PRJNA507245;
RNA-seq and sRNA-seq for HUVEC cells at 3 kPa and 30 kPa in the Gene Expression Omnibus (GEO) under accession codes GSE99686 and GSE11021;
sRNA-seq for HDF cells at 3 kPa and 30 kPa in the Gene Expression Omnibus (GEO) under accession codes GSE123008;
Proteomics results are reported as excel file Supplementary_table2.
All data is available with no restrictions. Source data plotted in figures can be found in supplemental table 8.

Field-specific reporting

Please select the best fit for your research. If you are not sure, read the appropriate sections before making your selection.

☒ Life sciences   ☐ Behavioural & social sciences   ☐ Ecological, evolutionary & environmental sciences

For a reference copy of the document with all sections, see nature.com/authors/policies/ReportingSummary-flat.pdf

Life sciences study design

All studies must disclose on these points even when the disclosure is negative.

Sample size	For fixed cell culture based assays, minimum sample size was chosen based on previously acquired data sets using power analysis so that a 10% change (in area, YAP, FA#) could be detected with 95% confidence. For live cell TFM experiments (n=15), sample size was chosen to allow for detection of a 30% change in total force with 95% confidence. For AFM measurements of stiffness, minimum sample size (n=25) was chosen based on previous tissue stiffness measurements (bovine meniscus) to allow for detection of a 20% difference in stiffness with 95% confidence. For Mass spec and HITS-CLIP, sample size was chosen to be 3 based on previously published data. For MRE-Sensor Seq, cell number collected for each bin was chosen so that enough material could be collected for illumina sequencing.
Data exclusions	No data was excluded
Replication	Once the protocols were established, all attempts of replication were successfully reproduced at least once and in most cases more than once (stated in methods and figure legends).
Randomization	Each cell culture experiment was performed by starting with a single population of cells that was randomly split after trypsinization into each experimental group. Fixed cell images were acquired by taking many (20-30) random fields of view. Fish experiments were performed on fish of each genotype, and for rescue experiments some fish from the AGO background were randomly chosen to be injected with human AGO for rescue.
Blinding	Authors were not blinded.

Reporting for specific materials, systems and methods

Materials & experimental systems

n/a	Involved in the study
☒	☐ Unique biological materials
☐	☒ Antibodies
☐	☒ Eukaryotic cell lines
☒	☐ Palaeontology
☐	☒ Animals and other organisms
☒	☐ Human research participants

Methods

n/a	Involved in the study
☒	☐ ChIP-seq
☐	☒ Flow cytometry
☒	☐ MRI-based neuroimaging

Antibodies

Antibodies used	Antibodies Used in Cultured Cells YAP (sc-10119, Santa Cruz, 1:200 IF) panAGO-2A8 antibody (MABE56, Millipore, 1:100 IP) AGO2 (2897, Cell Signaling, 1:200 IF, 1:2000 WB) Paxillin (ab32084, Abcam, 1:800 IF) RhoB (sc-8048, SantaCruz, 1:250 IF, 1:200 WB) CTGF (ab6992, Abcam, 1:200 IF, 1:1000 WB) Vinculin (V9131, Sigma-Aldrich, 1:200 IF, 1:2500 WB), STMN1 (ab52630, Abcam, 1:200 IF, 1:10000 WB) DROSHA (ab183732, Abcam, 1:5000 WB) GAPDH (2118, Cell Signaling, 1:4000 WB) Beta-Actin (sc-47778, SantaCruz, 1:2000 WB) anti-rabbit-HRP (7076P2, Cell Signaling, 1:4000 WB) anti-mouse-HRP (7074S, Cell Signaling, 1:4000 WB) Alexa-488 anti-rabbit (A-11008, ThermoFisher, 1:1000 IF) Alexa-647 anti-mouse (A-21236,ThermoFisher, 1:1000 IF) Antibodies Used in 3D Constructs Ago2 (2897, Cell Signaling, 1:2000 WB) beta-actin (ab8227, Abcam, 1:5000 WB) Vimentin (2897, Cell Signaling, 1:400 IF) phospho-Myosin light chain (ab2480, Abcam, 1:400 IF) Alexafluor-680 anti-mouse (A-21058, ThermoFisher, 1:15000 WB) Alexafluor-800 anti-rabbit (A32735, ThermoFisher, 1:15000 WB) Alexa-647 anti-rabbit (A-21245, ThermoFisher, 1:500) Antibodies Used in Zebrafish mouse anti-Phospho-Myosin Light Chain 2 (3671; Cell Signaling, 1:200 IF) mouse anti-Proliferating Cell Nuclear Antigen PCNA (clone PC10, M0879, Dako, 1:200 IF) rabbit anti-Fibronectin (F3648, Sigma, 1:200 IF) rabbit anti-Connective Tissue Growth Factor A (ab6992, Abcam, 1:150 IF) mouse anti-YAP (sc-10119, Santa Cruz Biotechnology, 1:200 IF) Alexa Fluor 488 anti-mouse (A-11034, ThermoFisher, 1:250 IF) Alexa Fluor 596 anti-rabbit (A-11037, ThermoFisher, 1:250 IF)
Validation	YAP antibody was purchased from Santa Cruz (sc-10119) and previously validated for IHC (Dupont, Nature 2011). Paxillin antibody [Y113] was purchased from abcam (ab32084) and has been extensively used and verified in the focal adhesion literature. panAGO-2A8 antibody was purchased from Millipore and validate per HITS-CLIP (Moore, Nature Protocols, 2014), more information are available from antibodypedia: https://antibodypedia.com/gene/27626/AGO2/antibody/554013/MABE56. AGO2 antibody was purchased from Cell Signaling(2897) and has been extensively used and verified: https://antibodypedia.com/gene/27626/AGO2/antibody/106152/2897. Vimentin antibody was purchased from Cell Signaling (3877) and has been extensively used and verified The RhoB, CTGF, Vinculin, STMN1, DROSHA, GAPDH, beta-Actin, Vimentin and Myosin light chain antibodies were verified by appropriate band size with western blot.

Eukaryotic cell lines

Policy information about cell lines

Cell line source(s)	293tx cells were purchased from Clontech Human Dermal Fibroblasts were purchased from ATCC (PCS-201-010, Lot#63014910) Human Umbilical Vein Endothelial Cells were purchased from Cell Applications Inc (200-05n, Lot#3051) Human Umbilical Arteries Endothelial Cells were purchased from Cell Applications Inc (202-05n)
Authentication	Human Dermal Fibroblasts were isolated from human neonatal foreskin tissue samples based on attachment and outgrowth on tissue culture plastic.

HUVECs were verified by Cell applications Inc to express VEGFR2, stain for EC-specific Dil-Ac-LDL and form vessel-like structures when cultured with HDF in the presence of VEGF.
HUAECs were verified by Cell applications Inc to express Factor VIII-related antigen and for EC-specific Dil-Ac-LDL and from the ability to attach and spread on tissue culture ware surface, and proliferate in Endothelial Cell Growth Medium.

Mycoplasma contamination	Yes, cells were tested and found to not have mycoplasma contamination.
Commonly misidentified lines (See ICLAC register)	No commonly misidentified cell lines were used in this study.

Animals and other organisms

Policy information about studies involving animals; ARRIVE guidelines recommended for reporting animal research

Laboratory animals	Wild-type (AB) Danio rario animals and ago2 mutant Danio rerio animals (Cifuentes, Science 2010) were raised and maintained at 28.5°C using standard methods and according to protocols approved by Yale University Institutional Animal Care and Use Committee (# 2015-11473)
Wild animals	No wild animals were used in this study.
Field-collected samples	No field collected samples were used in this study.

Flow Cytometry

Plots

Confirm that:

☒ The axis labels state the marker and fluorochrome used (e.g. CD4-FITC).

☒ The axis scales are clearly visible. Include numbers along axes only for bottom left plot of group (a 'group' is an analysis of identical markers).

☒ All plots are contour plots with outliers or pseudocolor plots.

☒ A numerical value for number of cells or percentage (with statistics) is provided.

Methodology

Sample preparation	Cells were trypsinized from surfaces, washed and resuspended in PBS without Calcium or Magnesium.
Instrument	BD FACSAria II
Software	BD FACSDIVA 7
Cell population abundance	To minimize the possibility of cells expressing multiple MRE-Sensors, cells were infected to achieve 10-20% of the population as GFP/RFP positive.
Gating strategy	FCS/SSC gate was set for single cells to exclude cell debris and doublets. GFP and RFP positive gates and compensation settings were determined using cells infected with only GFP or only RFP. Four sorting gates were set based on the 2 control plasmids (Empty-Sensor and miR125-Sensor). The upper limit bin (Not Suppressed) was designed to contain 90% or more events/cells infected with the Empty-Sensor and less than 0.5% of events for the miR125-Sensor. Vice versa, the lover bins (Strongly Suppressed and Suppressed) were designed to contain 90% of events coming from cells infected with miR125-Sensor, in a ratio close to 3:2 (~60% of events in Strongly Suppressed bin and ~40% of events in Suppressed). The 3th bin (Mildly Suppressed) represent the conjunction between the Not Suppressed and the Suppressed bins and derive for subtraction between the two bins. For clarity, the contour plot represents the total percentage of event in each single bins, grouped in "island" of 15% probability were shown for the Empty-Sensor, miR125-Sensor, Sensor-Library at 3 kPa and Sensor-Library at 30 kPa.

☒ Tick this box to confirm that a figure exemplifying the gating strategy is provided in the Supplementary Information.